Microwave Spectroscopy of Highly Underdoped Yttrium Barium Cuprate

by

Wendell A. Huttema
B.Sc., University College of the Fraser Valley, 2002

A THESIS SUBMITTED IN PARTIAL FULFILLMENT
OF THE REQUIREMENTS FOR THE DEGREE OF
MASTER OF SCIENCE
in the Department
of
Physics

SIMON FRASER UNIVERSITY
Spring 2006

APPROVAL

Name: Wendell A. Huttema

Degree: Master of Science

Title of thesis: Microwave Spectroscopy of Highly Underdoped Yttrium Barium Cuprate

Examining Committee: Dr. Karen Kavanagh
Chair

Dr. David M. Broun, Senior Supervisor
Assistant Professor, Department of Physics, SFU

Dr. J. Steven Dodge, Supervisor
Assistant Professor, Department of Physics, SFU

Dr. Michael E. Hayden, Supervisor
Associate Professor, Department of Physics, SFU

Dr. Malcolm Kennett, Internal Examiner
Assistant Professor, Department of Physics, SFU

Date Approved: December 6, 2005

SIMON FRASER UNIVERSITY library

DECLARATION OF PARTIAL COPYRIGHT LICENCE

The author, whose copyright is declared on the title page of this work, has granted to Simon Fraser University the right to lend this thesis, project or extended essay to users of the Simon Fraser University Library, and to make partial or single copies only for such users or in response to a request from the library of any other university, or other educational institution, on its own behalf or for one of its users.

The author has further granted permission to Simon Fraser University to keep or make a digital copy for use in its circulating collection, and, without changing the content, to translate the thesis/project or extended essays, if technically possible, to any medium or format for the purpose of preservation of the digital work.

The author has further agreed that permission for multiple copying of this work for scholarly purposes may be granted by either the author or the Dean of Graduate Studies.

It is understood that copying or publication of this work for financial gain shall not be allowed without the author's written permission.

Permission for public performance, or limited permission for private scholarly use, of any multimedia materials forming part of this work, may have been granted by the author. This information may be found on the separately catalogued multimedia material and in the signed Partial Copyright Licence.

The original Partial Copyright Licence attesting to these terms, and signed by this author, may be found in the original bound copy of this work, retained in the Simon Fraser University Archive.

Simon Fraser University Library
Burnaby, BC, Canada

Abstract

The manner in which the Mott insulating state gives way to superconductivity when the number of charge carriers is changed is one of the fundamental questions about high-T_c superconductors that remains unanswered. This is because of both the complexity of the high-T_c superconductors and the lack of experimental data on very clean underdoped samples. We have developed a novel technique for continuously varying the doping in a single sample of $YBa_2Cu_3O_{6+x}$ without changing the oxygen content. This allows us to access different dopings with transition temperatures between 0 K and 17 K. This thesis presents our data on the temperature and doping dependence of the superfluid density, which shows clear linear temperature dependence, typical of a good d-wave superconductor. An apparent phase transition as the doping is varied through a transition temperature of 11 K is discussed and evidence is shown for a small spectroscopic energy gap that is proportional to T_c.

Contents

Approval **ii**

Abstract **iii**

Contents **iv**

List of Figures **vi**

1 Introduction **1**

1.1 Cuprate Electrodynamics 4

2 Experimental Methods **6**

2.1 Gas Handling System 6

2.2 Cavity Perturbation Apparatus 8

2.2.1 Low Temperature Apparatus 10

2.2.2 Cavity Perturbation 14

2.2.3 Dielectric Resonators 15

2.2.4 Microwave Measurement Circuit 18

2.2.5 Calibration Measurements 20

3 The Chemistry of $\mathbf{YBa_2Cu_3O_{6+x}}$ **22**

3.1 Crystal Structure and Oxygen Ordering 22

3.2 Sample Preparation 26

4 Superfluid Density **27**

4.1 Surface Impedance 27

4.2 Conductivity 30

4.3 Strong Scattering Effects 31
4.4 Lack of a Kosterlitz-Thouless-Berezinski Transition 33
4.5 Temperature Slope of the Superfluid Density 34
4.6 Correlation Between T_c and ρ_{s0} 37
4.7 Phase Transition? 39

5 Microwave Conductivity **41**
5.1 Two-Fluid Analysis 41
5.2 Normal Fluid Fraction 43
5.3 Quasiparticle Transport Relaxation Rate 44

6 Conclusion **49**

A The Cavity Perturbation Approximation **50**

Bibliography **53**

List of Figures

1.1 Cuprate Phase Diagram 2

2.1 Back of the Gas Handling System (IronCAD and photo) 7
2.2 Photograph of the Front of the Actual Gas Handling System. 9
2.3 Magnetic Field Microwave Probe 12
2.4 Sample Field Lines in a Rutile Resonator 15
2.5 Bead-Pull Results From a Rutile Resonator 17
2.6 Measurement System 19
2.7 PbSn Reference Data 20

3.1 $YBa_2Cu_3O_{6+x}$ Crystal Structure 23
3.2 Oxygen Ordering Leading to Doping of Holes 24
3.3 T_c versus Doping and Oxygen Ordering Phases 25

4.1 R_s–X_s Matching Technique 28
4.2 Surface Impedance versus Temperature 29
4.3 Fluctuation Peak in σ_1 30
4.4 Sample Dependance of ρ_s 31
4.5 Low Temperature Behaviour of ρ_s 32
4.6 Superfluid Density for $YBa_2Cu_3O_{6.333}$ 33
4.7 Slope of ρ_s versus T_c 35
4.8 Anisotropy of the Normal Fluid Density 36
4.9 Linear Plot of T_c versus the Zero Temperature Superfluid Density 38
4.10 log-log Plot of T_c versus the Zero Temperature Superfluid Density 38
4.11 $\lambda^2(T = 0)/\lambda^2(T)$ versus T/T_c 39

5.1 Microwave Conductivity 42
5.2 Quasiparticle Conductivity Spectrum as a Function of T 43
5.3 f_n versus T 44
5.4 Scattering Rate versus Temperature 45
5.5 Scattering Rate for Numerous Cuprates 45
5.6 Illustration of Clean Limit vs. Dirty Limit in $\sigma_1(\omega)$ 47
5.7 2Δ versus T_c 48

Chapter 1

Introduction

For thirty years superconductivity was well explained by the theory of Bardeen, Cooper, and Schrieffer[9] (BCS) until, in 1986, Bednorz and Müller discovered superconductivity in $Ba_xLa_{5-x}Cu_5O_{5(3-x)}$[10]. Since that time over 100 cuprate superconductors have been discovered, with transition temperatures (T_c's) as high as 138 K at ambient pressure and over 150 K under pressure. Superconductivity in this new class of materials cannot be explained in the framework of BCS theory and a number of different theories have been brought forward[44].

Part of the mystery of the high temperature superconductors is the way their physical properties change as a function of charge carrier concentration. Carrier concentration can be tuned chemically in almost all high temperature superconducting materials, a process known as doping.

An experimental phase diagram for the hole doped cuprate superconductors is shown in Fig. 1.1. The T_c at optimal doping is labeled as well as the doping for optimal T_c and for superconductivity to disappear on the underdoped side. The doping is expressed in terms of the number of holes per CuO_2 in the planes (see chapter 3 for further details).

The band structure of the cuprates suggests they should be metallic at zero doping[42, 58]. However, strong coulomb repulsion forces electrons to singly occupy available sites, completely blocking motion and resulting in a Mott insulating phase in which the electronic spins all align antiferromagnetically. As holes are doped into the system (see chapter 3) mobility is increased and superconductivity emerges at low temperatures. At low dopings the pseudogap phase is encountered, where superconductivity occurs at low temperatures. If the hole doping is further increased the superconducting T_c increases to a maximum of

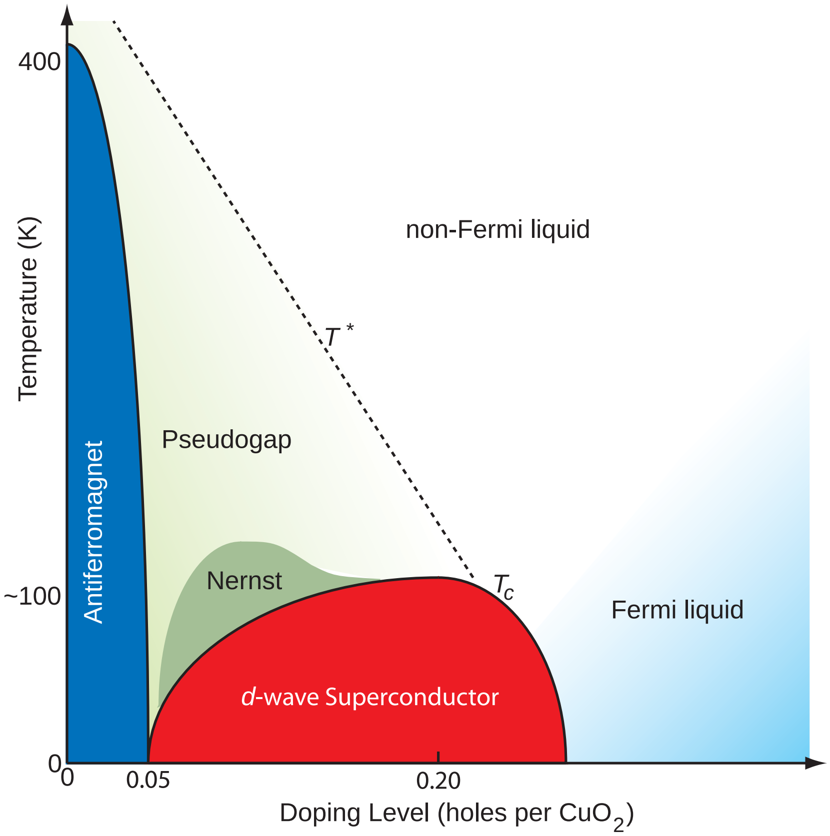

Figure 1.1: Phase diagram for the hole-doped cuprates.

about 93.5 K at optimal doping before dropping to under 90 K for $YBa_2Cu_3O_7$. In other cuprate superconductors the doping can be increased until superconductivity is lost and the material becomes metallic.

The large coulomb repulsion in the cuprates also leads to a pairing state for charge carriers that is d-wave in character, rather than the conventional s-wave pairing seen in most other superconductors. The coulomb energy of an electron pair is reduced because the probability for the electrons in a d-wave Cooper pair to be at the same site is vanishingly small. Evidence for d-wave pairing was first provided by measurements of the in-plane penetration depth[24], where a linear low temperature behaviour was observed, typical of an order parameter with nodes. As there are nodes in the superconducting gap at the Fermi surface there are quasiparticles with arbitrarily low energies that can destroy the superconductivity. This should be compared with an s-wave gap which is isotropic everywhere on the Fermi surface and thus can only have quasiparticle excitations when the gap energy is exceeded, resulting in exponential temperature dependence of the superfluid density at low temperature. The most compelling evidence for d-wave pairing came from phase-sensitive tests of the order parameter by Tsuei *et al.*[53] which showed that the gap function does indeed change sign in the same way as a $d_{x^2-y^2}$ orbital.

The order parameter for superconductivity is a complex quantity with both an amplitude and a phase. In BCS theory the phase of the order parameter is unimportant; the transition temperature is related only to the amplitude of the order parameter, which is often equated to the superconducting gap Δ. In the underdoped cuprate superconductors the superfluid density, which is the energy scale for phase fluctuations, is very low. This has led to proposals that it is not the amplitude of the order parameter that determines the transition temperature in the cuprates, but rather the onset of long-range phase order[19, 22, 23, 26, 25]. In this case superconductivity would persist *locally* above T_c, with long-range phase coherence suppressed by fluctuations in the phase of the order parameter. Measurements of a strong Nernst effect above T_c have been interpreted by Xu et. al.[57] as evidence of pairing. The Nernst effect is observed my measuring the voltage transverse to a thermal gradient in the presence of a magnetic field applied perpendicular to the CuO_2 planes. The Nernst effect is known to be strong in superconductors, because the magnetic flux is tied to vortices, which drift along a thermal gradient. A moving vortex induces a transverse voltage. The observation of a Nernst signal that persists above T_c would imply that cooper pairs also persist above T_c. The approximate region in which a strong Nernst signal is seen is labeled in Fig. 1.1.

Microwave frequency measurements are able to determine the effective superfluid density (Ch. 4), one of the fundamental thermodynamic variables of a superconductor. This makes these measurements extremely useful for distinguishing between different theoretical viewpoints. At the same time, sample quality among the cuprate superconductors has been an issue and has resulted in a number of theoretical missteps. Microwave measurements are very susceptible to sample quality, allowing intrinsic effects to be easily separated from those due to sample defects. There are a number of issues associated with poor sample quality. Disorder and extended defects, such as cracks, lead to extra pairbreaking, which lowers the superfluid density, and to nonlinear effects in the microwave response, which limits the input power that can be applied to a sample.

Another difficulty that is encountered is related to doping homogeneity. There are two regions of the $\mathrm{YBa_2Cu_3O_{6+x}}$ phase diagram where plateaus exist in the T_c for a given oxygen content. These plateaus occur at T_c's of $\tilde{9}0$ K and $\tilde{6}0$ K. Away from these plateaus it is very difficult to produce samples with sharp superconducting transitions[38, 39].

Recently, Drs. Liang, Bonn and Hardy have succeeded in producing samples with with sharp superconducting transitions, and we have also harnessed the process of CuO-chain ordering to fulfill a long-held ambition in strongly correlated electron materials – continuous tunability of the carrier density in a *single* sample, with *no* change in cation disorder[31]. This has allowed us to study the doping dependence of the superfluid density and the microwave conductivity without the complication of sample-to-sample variations.

The cuprate superconductors are very anisotropic, and are often treated as two-dimensional. A strictly two dimensional superconductor should not exist, as the Mermin-Wagner theorem states that phase transitions in systems with a continuous degree of freedom in two dimensions can only occur at $T = 0$. However, below the Kosterlitz-Thouless transition the superfluid density is finite. In the cuprates vortices will be bound together below the Kosterlitz-Thouless-Berezinski transition temperature T_{KT} defined by

$$k_B T_{KT} = \frac{\pi \hbar^2 d}{8 e^2 \mu_0 \lambda^2 (T_{KT})} \; , \tag{1.1}$$

where $\lambda = \sqrt{m/\mu_0 n_s e^2}$ is the London penetration depth and n_s is the number of superconducting charge carriers, of mass m and charge e. Above T_{KT}, however, the entropy gain of having two vortices moving independently can offset the energy cost of them moving apart resulting in a gain in the free energy for unbound vortices. This results in the superfluidity disappearing at T_{KT}.

1.1 Cuprate Electrodynamics

Microwave spectroscopy is a powerful probe of the long-wavelength response of solids. It is especially useful for superconductors, in which the d.c. resistivity is shorted to zero by supercurrents. At microwave frequencies the conductivity of a superconductor remains finite but becomes complex, developing an out-of-phase component because of the purely reactive response of the super-electrons. In the Meissner state, magnetic fields are excluded from the bulk of the sample as described London and London in 1935[41]. The second London equation,

$$\nabla \times (\mu_0 \lambda^2 \mathbf{J}_s) = -\mathbf{B} \; , \tag{1.2}$$

where $\mathbf{J}_s$ is the supercurrent density and $\mathbf{B}$ is the applied magnetic field, leads directly to a screening equation for the magnetic field in a superconductor,

$$\nabla^2 \mathbf{B} = \frac{\mathbf{B}}{\lambda^2} \ . \tag{1.3}$$

In this regime the utility of microwave spectroscopy lies in the dual character of the complex conductivity $\sigma = \sigma_1 - \mathrm{i}\sigma_2$. The real part σ_1 contains details of the scattering dynamics of thermally excited quasiparticles, or 'normal' electrons, while the imaginary part σ_2 acts as a thermodynamic probe of the electronic excitation spectrum. It is proportional to the superfluid density, which is a thermal equilibrium property that can be obtained directly from the free energy.

For microwave spectroscopy of conducting materials the experimentally accessible quantity is the surface impedance, the ratio of the transverse components of the electric and magnetic fields at the surface of the sample. The surface impedance is a complex quantity, $Z_s = R_s + \mathrm{i}X_s$, and can be inferred from a measurement of the frequency and line-width of a resonant mode in a resonant cavity as shown in Chapter 2. In the cuprates we normally have the coherence length $\xi_0 \ell \lambda$ and the mean free path $l \ell \lambda$, which puts them in the local limit where current density at a point is determined by the local value of electric field. In this case the conductivity is related to the surface impedance by the local-limit expression

$$\sigma = \mathrm{i}\omega\mu_0 / Z_s^2 \ , \tag{1.4}$$

where ω is the angular frequency at which the measurement takes place.

At finite frequencies the normal excitations conduct in parallel to the superfluid and can be represented by a Drude conductivity[30, 32]. The electrodynamics of the normal and superfluid carriers can then be incorporated into a two-fluid model of the complex conductivity[55],

$$\sigma = \sigma_1 - \mathrm{i}\sigma_2 = \frac{ne^2}{m} \left[\frac{f_s}{\mathrm{i}\omega} + \frac{f_n}{1/\tau + \mathrm{i}\omega} \right] \ , \tag{1.5}$$

where f_n and f_s represent the fraction of electrons which are normal and superfluid respectively, with $f_n + f_s = 1$ as required in the clean limit by the oscillator strength sum rule, n is the total number of electrons, and $1/\tau$ is the quasiparticle transport relaxation rate.

Chapter 2

Experimental Methods

Cavity perturbation measurements on a small superconducting single crystal of $YBa_2Cu_3O_{6.333}$ were performed using a rutile dielectric resonator. The apparatus was designed and built by Dr. D. Broun and Dr. W. Hardy at the University of British Columbia. In order to use the apparatus at S.F.U., a number of things were needed, including a gas handling system, which I built and cryostat which I helped to set up.

Considerable time was also spent characterizing two different rutile resonators. Usable resonant modes must be searched for using an Agilent 8722ES vector network analyzer and their position dependence mapped out as discussed in Sec. 2.2.3. Finding modes that can be used in the experiments is very time consuming, as, for example, the one resonator has more than 200 resonant modes between 2.64 and 14 GHz, but only four of them can be used. I have also examined the temperature dependence of the resonant frequency and optimized some of our temperature control and additionally, I have designed an enclosure for a new, larger rutile dielectric resonator.

2.1 Gas Handling System

My first project upon joining Dr. Broun's laboratory was to design and build a gas handling system. The main purpose of this system was to allow us to regulate the vapour pressure of a liquid helium bath, which in turn sets the temperature of the bath. It was also designed to allow us to easily connect other lines, for such things as a cold trap. One of the constraints on our system was that we wanted it to be mobile. Instead of a large system, typically set up on a 4 by 4 foot sheet of plywood, we wanted to fit our system into a scientific rack,

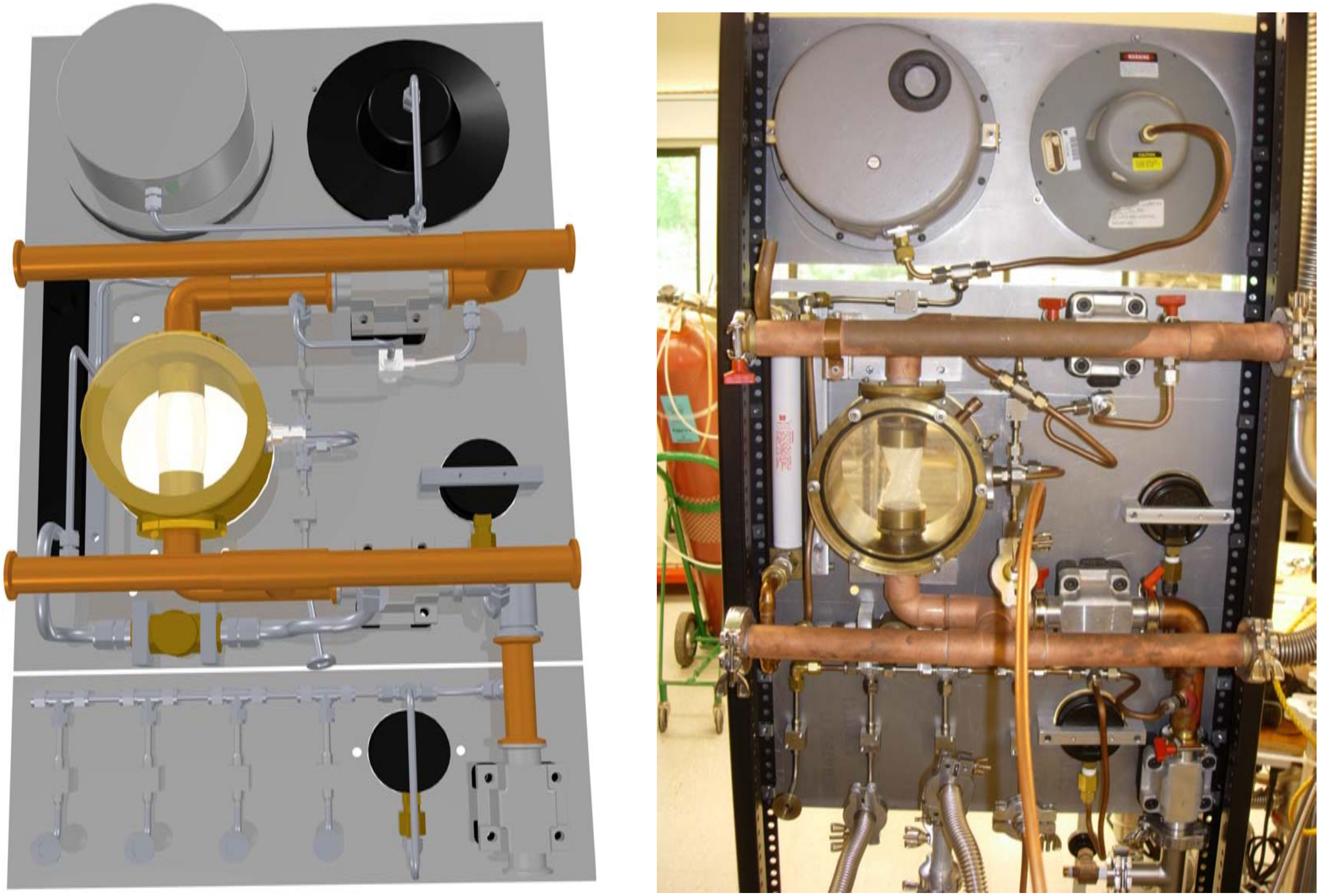

Figure 2.1: The figure on the left is an IronCAD drawing showing the back of the design of gas handling system, while the figure on the right is a photograph of the back of the actual gas handling system.

about 19 inches wide by 6 feet tall. We also wanted the system to be easily accessible and visible, which meant not using the bottom of the rack for gauges or valves. This further reduced our usable space to about 19 inches by 3 feet.

To ensure that it was even possible to fit a gas handling system in such a small space, I first drew up a design of the system in IronCAD, a 3 dimensional computer assisted drafting (3D CAD) program. Figure 2.1 shows a back view of the IronCAD design of the gas handling system and a back view of the actual system. These pictures show the complexity of the system, while Fig. 2.2, which is of the front of the actual gas handling system, shows the simplicity of the completed system.

2.2 Cavity Perturbation Apparatus

Cavity perturbation techniques can be used for very accurate determinations of the surface impedance of metals and superconductors, and bypass some of the difficulties presented by other types of measurements. An optical-type reflectivity experiment can in principle yield the surface impedance, however the reflectivity is indistinguishable from unity in metals and superconductors, and, at microwave frequencies, is further complicated by diffraction effects, as the wavelength becomes comparable to the size of a typical sample. Another possibility is to attach leads directly to the sample as in low-frequency measurements. This is also problematic at microwave frequencies since the impedance of the sample is only a fraction of an ohm, which is comparable to the contact resistance and difficult to match to the characteristic impedance of a microwave transmission line.

Cavity perturbation avoids the limitations above, and thus has been widely adopted for microwave measurements. In cavity perturbation the sample is treated as part of the inner surface of a high quality factor (high-Q) resonator. The resonator amplifies the interaction of the electromagnetic radiation with the sample by the Q factor, through repeated reflection of the fields. This also multiplies up the signal and provides effective impedance matching to the external transmission lines. As a result, the resolution of the experiment improves with the Q of the resonant mode, allowing very low loss samples (i.e. superconductors) to be characterized. The resonator also creates spatially well-defined fields, simplifying geometric effects. Choice of the resonant mode determines the polarization of the microwave field, allowing it to be lined up with a principal axis of a single-crystal sample. The surface impedance can be simply determined through measurements of the frequency and line-width

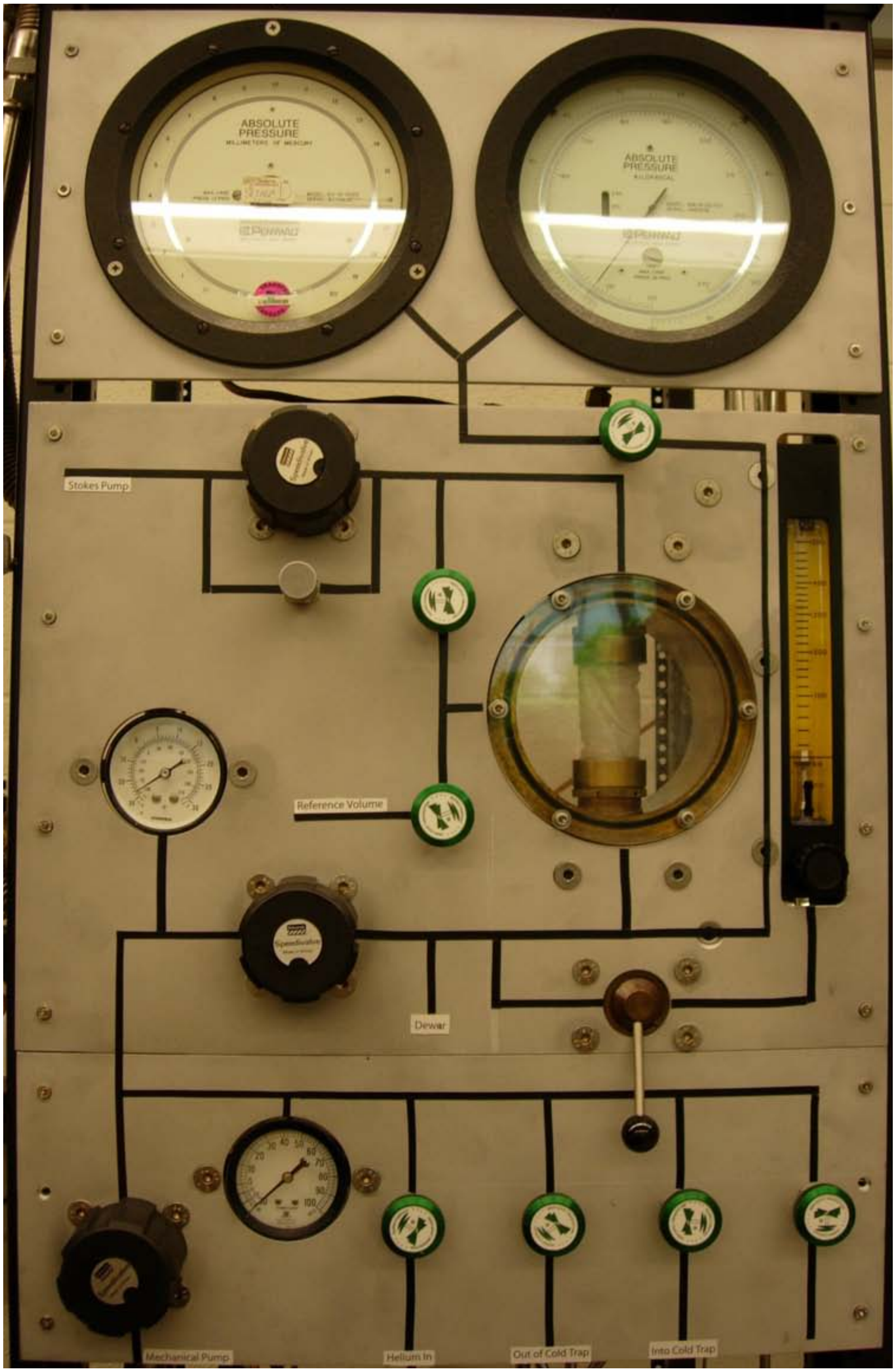

Figure 2.2: Photograph of the Front of the Actual Gas Handling System.

of the resonant mode as shown in Section 2.2.2.

The best quality samples of cuprate superconductors tend to be small single crystals, often less than a millimetre in size. Even cavity perturbation measurements on such samples can be difficult due to their low microwave absorption and because they make up a very small fraction of the area of the resonator walls. One of the innovations adopted to solve these problems was the sapphire hot-finger technique[51] which allows the sample to be heated independently of the resonator. This allows the resonator temperature to be held constant in a helium bath for the duration of an experiment, with the result that all changes in frequency and line-width can be attributed to the sample's surface impedance.

Superconducting resonators, made of materials such as bulk niobium metal[51], or from copper with a superconducting coating, such as a PbSn alloy[12, 16], are often used for cavity perturbation, but have a number of limitations. Any joints in the apparatus tend to act as superconducting weak links, limiting operation to low power. The quality of these resonators also tends to degrade over time due to oxidation of the surface of the superconductor. Also, superconducting resonators cannot be used in high magnetic fields as they would either be driven normal or into a highly dissipative state of flux flow.

2.2.1 Low Temperature Apparatus

The design for the cavity-perturbation apparatus is constrained by several requirements. It needs a mechanically rigid mount for the dielectric resonator that puts the resonator in good thermal contact with the helium bath. The resonator must be surrounded by a metallic enclosure, to prevent radiation losses, but the walls of the enclosure have to be kept well away from the resonator to minimize conduction losses. The enclosure must contain two coupling ports, so that microwaves can be coupled through the resonator in transmission, and allow access for the sample, mounted on a sapphire hot finger. As the hot finger and sample will be heated to temperatures in excess of 200 K, the space inside the enclosure has to be kept under high vacuum. Working in high magnetic fields places further constraints on the design. The apparatus described here fits inside a standard $2''$ diameter magnet bore, tightly restricting the space available. Temperatures below 4.2 K are reached in this apparatus with a miniature 1 K pot operating in one-shot mode to cool the sample thermal stage. In addition, the design includes a feature that is very desirable in cavity perturbation — a movable sample stage that allows the sample to be completely withdrawn from the resonator. This is done in this system by moving the whole assembly of 1 K pot and sample thermal stage. As a result, the background microwave absorption of the resonator can be measured directly, allowing the *absolute* microwave absorption of the sample to be determined *in situ*.

The low temperature end of the apparatus is shown in Fig. 2.3. The cylindrical dielectric resonator, with an access hole bored down the cylinder axis, is mounted with GE varnish onto a sapphire plate that suspends it inside the copper enclosure. The strength and high thermal conductivity of sapphire ensure rigid mounting and good thermal contact between the resonator and helium bath. A pair of $0.141''$ stainless-steel coaxial lines run the length of the insert and terminate in loops near the cavity. Microwaves are coupled to the resonator through a pair of coupling ports in the sides of the enclosure. The amount of coupling can be varied by adjusting the vertical position of the coaxial lines, which enter the vacuum space through room-temperature sliding o-ring seals. In this experiment the maximum coupling is limited by the size of the coupling holes, typically to about 2% of critical coupling, where critical coupling corresponds to impedance matching the coax line to the resonator. The position and orientation of the coupling loops is usually optimized to operate at maximum coupling, as this improves signal strength and frequency stability. It was found in early experiments that the Teflon dielectric in the coaxial cables allowed a slow gas leak from room temperature, which, if left unchecked, degraded the operation of the thermal stage. These leaks were eliminated by coating the ends of the coaxial lines, including the coupling loops, with Stycast 2850 black epoxy. A small charcoal sorption pump attached to the base of the copper enclosure further ensures high cryogenic vacuum for the duration of the experiment.

The temperature of the sample is controlled using a sapphire hot finger connected to a small, isothermal sapphire platform that is weakly thermally connected to the base of the 1 K pot by a thin-walled quartz tube. The sample temperature is measured with a Cernox thermometer[1], and is regulated between 1.1 K and 200 K by a Conductus/Neocera LTC-20 temperature controller. The precision of the temperature control is 10^{-4} K below 10 K and 2×10^{-3} K at the highest temperatures. Wiring to the thermal platform (not shown in Fig. 2.3) passes through the 1 K pot for optimal thermal anchoring, and there is no discernible heat leak from room temperature into the thermal stage. Electrical feedthroughs between the helium and vacuum spaces are made with brass wires, sealed with Stycast 2850 epoxy as they pass through the copper base of the 1 K pot. The entire thermal stage, including the 1K pot, is movable, allowing the sample to be completely withdrawn from

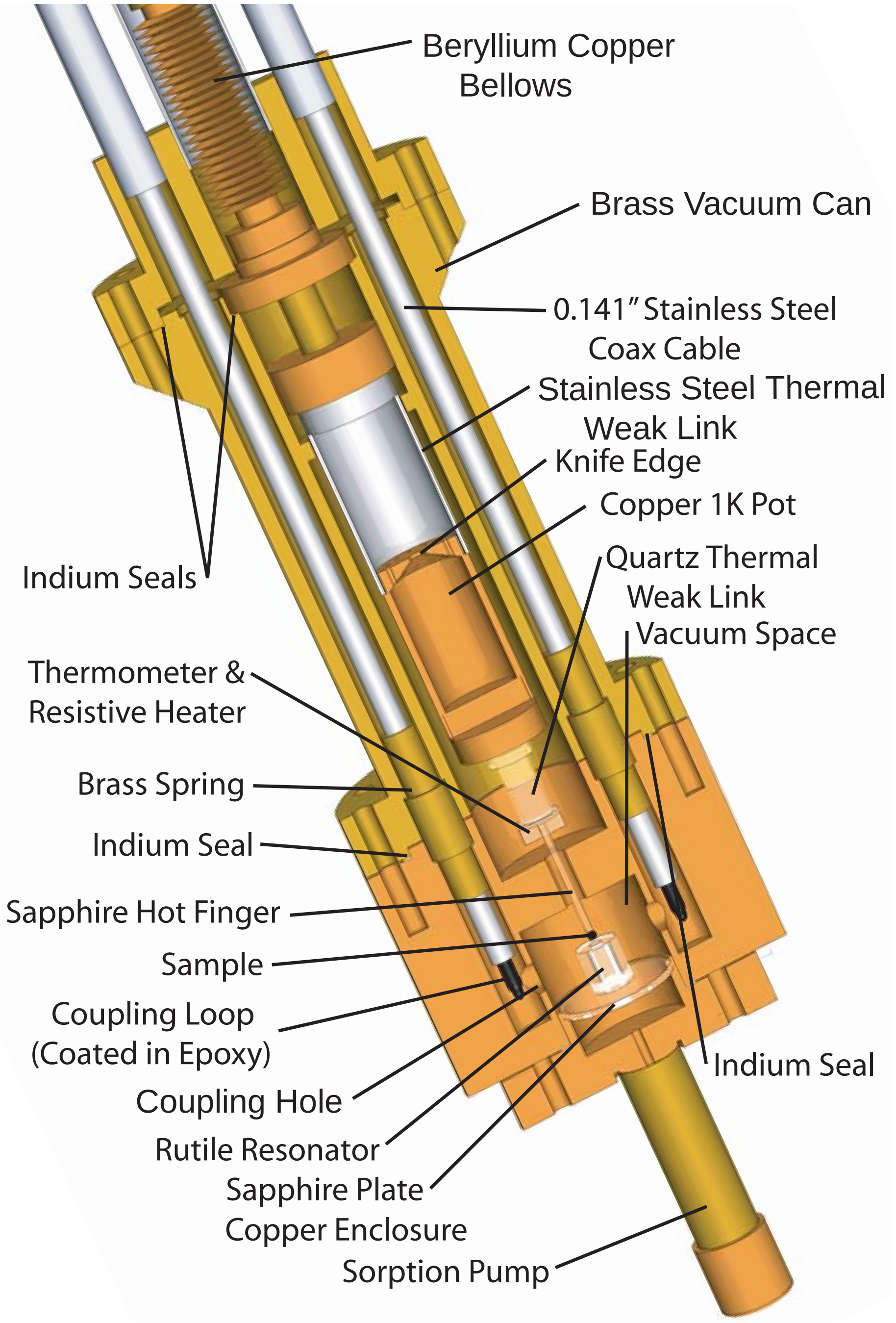

Figure 2.3: A cut-away schematic of the low temperature end of the cavity perturbation apparatus. The 5.49 GHz rutile resonator is shown inside the copper enclosure, the outside of which is in direct contact with the helium bath at 4.2 K. A movable sample thermal stage is one of the novel features of the design, consisting of an independently heated sapphire hot finger mounted below a movable 1 K refrigerator. A key component of the motion stage is the flexible vacuum seal provided by a pair of BeCu bellows housed inside the 1 K pot pumping line, separating it from the vacuum space.

the resonator for background calibrations. To permit motion while maintaining a hermetic seal between the 1 K pot pumping tube and the vacuum space, flexible BeCu bellows[2] are used. The motion is controlled by a stainless steel rod that runs up the inside of the 1 K pot pumping line and passes through a sliding o-ring seal at room temperature. A ledge in the 1 K pot housing provides positive location for the sample stage when it is in the fully engaged position.

The 1 K pot is constructed in two parts to avoid thermal losses associated with superfluid film creep. The lower section is made from copper and has a volume of 1.9 ml. The upper section is a tube made from $0.001''$ stainless-steel shim stock that acts as weak thermal link to 4.2 K. The two sections are connected by a small, circular orifice, 0.5 mm in diameter with knife-like edges, that interrupts superfluid film flow. The 1 K pot is operated in one-shot mode, with a charge of helium provided by connecting the 1 K pot to a supply of high-purity helium gas that liquifies to fill the lower section of the pot. The 1 K pot has a better base temperature and longer hold time if the inside surfaces are assiduously kept free of contamination. An important part of this process is to pass the helium gas through a liquid nitrogen cold trap before it enters the apparatus in order to scrub it clean of impurity gases. With these precautions, boil-off from the 1 K pot is low enough that it can be pumped with a small turbo-molecular pump down to pressures below 10^{-3} mbar. For operation below 4.2 K, a typical hold-time for the 1 K pot is 10 hours, with a base temperature below 1.1 K. When operating above 4.2 K a small overpressure of helium gas is kept in the 1 K pot pumping line to ensure a reproducible thermal environment in the 1 K pot.

Sample interchange is performed with the low temperature insert warmed to room temperature. The copper resonator enclosure is unbolted from the brass vacuum can at the second lowest indium seal and removed. This gives direct access to the sapphire hot finger and thermal stage. Several precautions are taken to protect the delicate hot-finger assembly during this procedure. Before working near the sapphire rod, an aluminum mounting jig is brought into position and bolted into place on the indium flange at the bottom of the brass can. Two $\frac{1}{8}''$ diameter brass guide pins, which protrude $2''$ from the base of the brass can provide alignment for both the mounting jig and the resonator enclosure. These work by mating with corresponding clearance holes drilled vertically through the jig and enclosure, guaranteeing alignment to better than 0.1 mm. The sample to be measured is attached to the sapphire hot finger with a small amount of high vacuum grease[3], which provides good thermal contact and has negligible microwave absorption. The sample is mounted so that it sits at the center of the resonator with the 1 K pot stage in the fully engaged position. This position is a local maximum in the on-axis microwave magnetic field intensity, as described in Section 2.2.3. Siting the sample in this way enhances field uniformity and minimizes the contribution of sapphire thermal expansion to resonator frequency shift.

2.2.2 Cavity Perturbation

Cavity perturbation is a method for relating changes in the free response of a high Q resonator to changes in the surface impedance Z_s, the permittivity ϵ and the permeability μ of small samples placed inside. As shown in the Appendix, the main cavity perturbation result is:

$$\begin{aligned}\Delta f_0 + i\Delta f_B/2 \approx \Big\{ & \frac{i}{2\pi}\int_S \Delta Z_s \mathbf{H_1}\cdot\mathbf{H_2}\mathrm{d}S \\ & - f_0\int_V [\Delta\mu \mathbf{H}_1\cdot\mathbf{H}_2 + \Delta\epsilon' \mathbf{E}_1\cdot\mathbf{E}_2]\mathrm{d}V\Big\}\Big/4U. \end{aligned} \tag{2.1}$$

Here Δf_0 and Δf_B are the perturbative shifts in resonant frequency and the half-power bandwidth, respectively, and U is the electromagnetic energy stored in the resonator. $\mathbf{E}$ and $\mathbf{H}$ are complex phasor amplitudes of the electromagnetic fields, and the subscripts 1 and 2 denote the configurations before and after the perturbation. The prime on the permittivity indicates that conduction currents have been folded into a redefinition of the dielectric response, for mathematical convenience.

In our experiments the perturbation is caused by the presence of the sample and sapphire hot-finger, and is due to either a shift in sample temperature or a change in position. For surface impedance measurements on conductors the sample is inserted into the resonator along a node in the electric field. As a result, once the sample is fixed in place, the volume integral term in Eq. 2.1 can usually be ignored, and the cavity perturbation formula reduces to

$$R_s(T) + i\Delta X_s(T) \approx \Gamma[\Delta f_B(T)/2 - i\Delta f_0(T)]. \tag{2.2}$$

Here $\Gamma = 8\pi U/\int_S \mathbf{H}_1\cdot\mathbf{H}_2\mathrm{d}S$ is the resonator constant, which can typically be determined to an accuracy of 2.5% using replica samples of known surface impedance. $\Delta f_B(T)$ is the change in bandwidth on inserting the sample at temperature T into the empty resonator, and $\Delta f_0(T)$ is the shift in resonant frequency on warming the sample from the base temperature to temperature T. It is never possible to determine the absolute reactance by inserting the sample, because in doing so the magnetic permeability term in Eq. 2.1 gives a large frequency

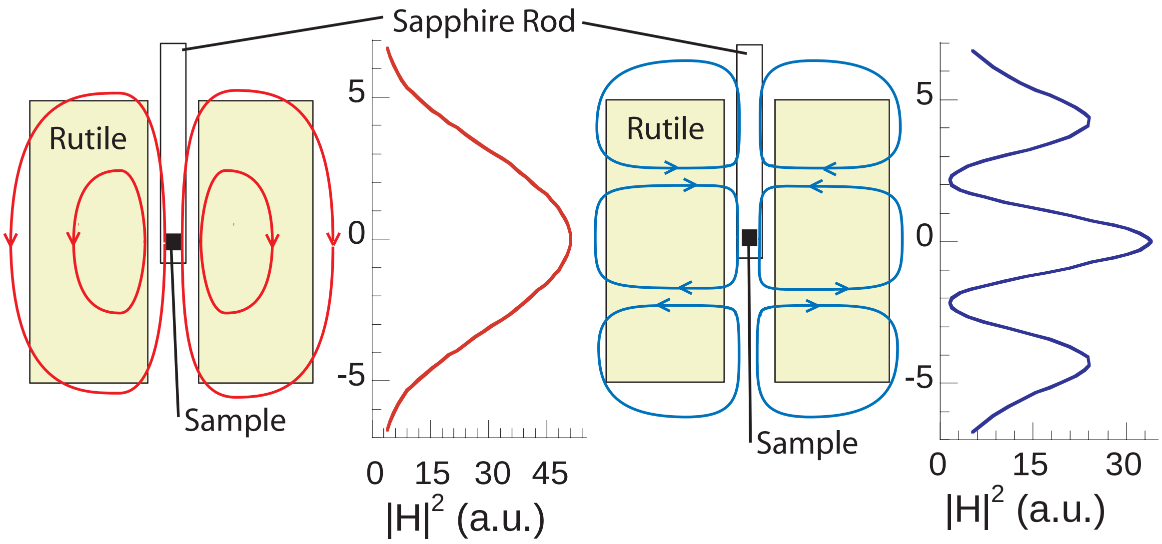

Figure 2.4: An illustration of the magnetic field structure of the $\mathrm{TE}_{01(n-\delta)}$ modes, for $n = 1$ and $n = 3$. The subscript $n - \delta$ specifies the number of half wavelengths of the TE_{01} waveguide mode along the z direction. The $\mathrm{TE}_{01(1-\delta)}$ mode is sketched on left side of the diagram, with the $\mathrm{TE}_{01(3-\delta)}$ mode to the right. Alongside each illustration is a plot of the experimentally determined magnetic field intensity $|H|^2$, for the larger rutile resonator. The $|H|^2$ data were obtained from the change in bandwidth on inserting the sample, using the bead-pull procedure described in the text.

shift that dwarfs the contribution from surface reactance, however it is possible to set the absolute surface resistance.

2.2.3 Dielectric Resonators

The resonators for this experiment were fabricated from oriented single crystals of rutile-phase $\mathrm{TiO_2}$. Rutile was chosen as the dielectric material because of its high dielectric constant, $\epsilon_r \approx 120$, and its low loss tangent, $\tan\delta \approx 3 \times 10^{-8}$. For a given frequency, the linear size of a dielectric resonator shrinks as $1/\sqrt{\epsilon_r}$, with a corresponding increase in filling factor that increases as $\epsilon_r^{3/2}$. For high ϵ_r material, displacement currents are very efficient at confining the microwave fields, reducing the magnitude of lossy conduction currents in the walls of the resonator enclosure. The low loss tangent results in quality factors well in excess of a million.

The specific resonator used in my experiments is a single-crystal rutile cylinder of radius 2.56 mm and height 5.9 mm, with a 1.5 mm diameter through hole bored along the axis. The crystalline c-axis is aligned with the cylinder axis to better than one degree, which is important because rutile is strongly birefringent. The raw single-crystal material for this resonator was supplied by eSCeTe[4], and was ground and polished to shape by Microlap Technologies[5]. The fundamental frequency of this resonator is 5.49 GHz, and it has a Q of 1.1×10^6 at 4.2 K. Another resonator in use in our lab is larger, with diameter=height=10 mm, and a 3 mm diameter bore along the cylinder axis. The fundamental resonance of this resonator is at 2.64 GHz and it has a Q of 1.7×10^6 at 4.2 K. Both the single-crystal growth and the resonator fabrication were carried out by ELAN[6].

The resonator modes used in these experiments are transverse electric modes with cylindrical symmetry, denoted $\mathrm{TE}_{01(n-\delta)}$ modes. These are desirable for several reasons. The electric field has a line node along the cylinder axis, minimizing the interaction of the sample and sapphire hot finger with electric fields. For the odd-order modes, the on-axis microwave magnetic field has maximum intensity at the center of the resonator. The $\mathrm{TE}_{01(1-\delta)}$ and $\mathrm{TE}_{01(3-\delta)}$ modes are sketched in Fig. 2.4, showing the sample located at an antinode of the microwave magnetic field.

Modes are identified using the movable sample stage to carry out a so-called “bead-pull” experiment. Although this only probes the fields along the resonator axis, it provides sufficient information to locate the $\mathrm{TE}_{01(n-\delta)}$ modes. To see how this works, Eq. 2.1 is broken into separate expressions for the shift in resonant frequency and bandwidth. Keeping only the dominant contributions, the small dielectric loss of the sapphire hot-finger is ignored and the magnetic field is assumed to be completely excluded from the interior of the conducting sample, making its effective permeability $-\mu_0$. Then

$$\Delta f_0 \approx \frac{f_0}{4U}\left\{\int_{\text{sample}}\mu_0\mathbf{H}_1\cdot\mathbf{H}_2\mathrm{d}V - \int_{\text{sapphire}}\epsilon_r\epsilon_0\mathbf{E}_1\cdot\mathbf{E}_2\mathrm{d}V\right\} \tag{2.3}$$

$$\Delta f_B \approx \frac{1}{4\pi U}\int_{\text{sample}}R_s\mathbf{H}_1\cdot\mathbf{H}_2\mathrm{d}S. \tag{2.4}$$

Here the changes in f_0 and f_B are with respect to the response of the empty resonator. The presence of a conducting sample reduces the effective volume of the resonator and increases its frequency. The sapphire hot-finger has the opposite effect and, due to its large volume in comparison to the sample, gives a large negative frequency shift for any mode not having an electric field node along the cylinder axis. Most candidate modes can immediately be ruled out using this criterion alone. Additional information is provided by the bandwidth, which for a conducting sample gives a clean measure of the magnetic field intensity. Representative

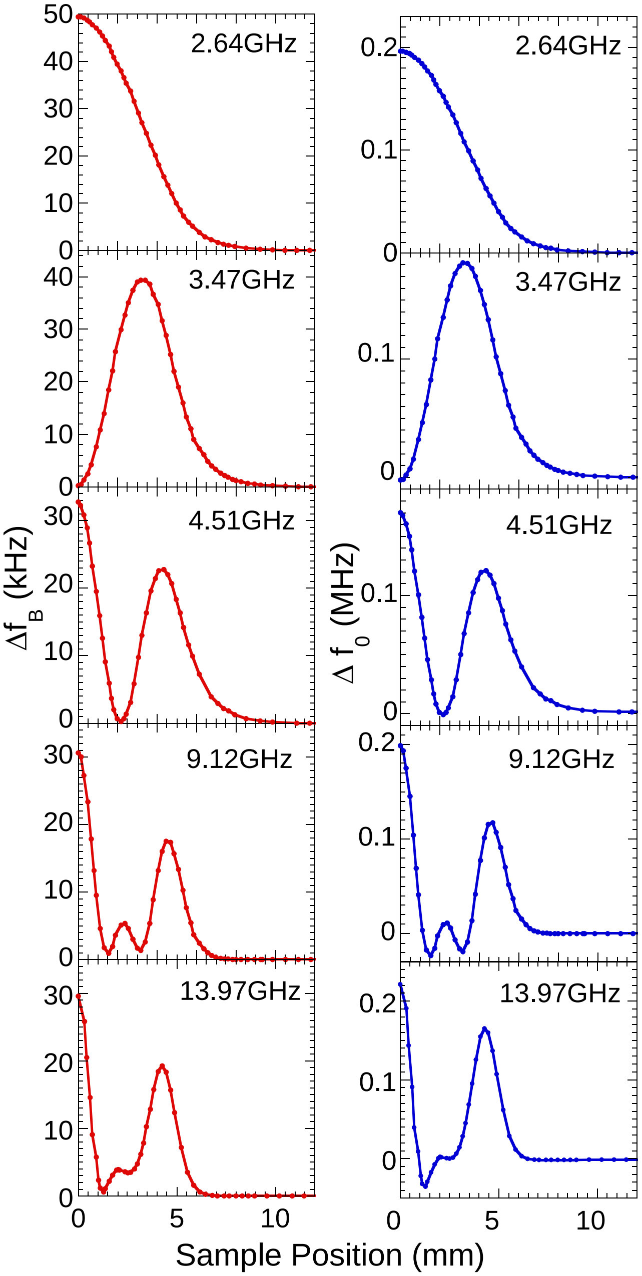

Figure 2.5: Bead-pull results for a number of useful modes of the larger rutile resonator. Δf_B is the change in resonant bandwidth on inserting a small $\mathrm{YBa_2Cu_3O_{6.333}}$ sample, in the normal state at 30 K, into the resonator. Δf_0 is the shift in resonant frequency with respect to the empty resonator. As described in the text, $\Delta f_B(z)$ gives a map of the magnetic field intensity along the axis. $\Delta f_0(z)$ provides similar information, but contains a term due to the interaction of the sapphire hot finger with the electric fields of the resonator. This term should be small for modes with an electric node along the cylinder axis.

data are presented in Fig. 2.5 for the larger resonator, showing results for modes at 2.64, 3.47, 4.51, 9.12 and 13.97 GHz. The empty resonator Qs of these modes are 1.73, 5.02, 6.0, 1.95 and 1.47 million respectively at 4.2 K. Plots of $|H|^2$ vs. position obtained from the Δf_B data are shown alongside the mode sketches in Fig. 2.4. A final confirmation of the field polarization comes from the use of a crystal of high-T_c superconductor as the test sample. The strong anisotropy of its electrodynamic response allows us to verify that the microwave magnetic field at the center of the resonator is indeed parallel to the cylinder axis.

2.2.4 Microwave Measurement Circuit

In these experiments the response of the resonator modes is probed in transmission, using an Agilent 8722ES vector network analyzer (VNA). The VNA is set up to detect the scattering parameter $\tilde{S}_{21}(f)$, the complex transmission amplitude through the microwave circuit. For the free decay of a high Q resonance, the dominant contribution to $\tilde{S}_{21}(f)$ is a simple pole at the complex decay frequency,

$$\tilde{S}_{21}(f) \sim \frac{1}{f - (f_0 + i f_B/2)}. \tag{2.5}$$

A direct, non-resonant transmission amplitude $\tilde{D}_{21}$ acts in parallel with the resonant coupling. The model used to fit to the measured scattering amplitude is therefore

$$\tilde{S}_{21}(f) = \frac{\tilde{S}^0_{21}(f)}{1 - 2i(f - f_0)/f_B} + \tilde{D}_{21}, \tag{2.6}$$

where $\tilde{S}^0_{21}$ is the transmission amplitude on resonance. Tildes denote complex quantities.

A LabVIEW routine, programmed by Dr. D. Broun and B. Morgan, processes the scattering parameter data from the VNA, fitting to them using a complex-valued Levenberg–Marquardt routine based on code from *Numerical Recipes in C*[48]. This is an improvement over routines that fit only to the *amplitude* of the resonant response — retaining the phase signal doubles the amount of information in each trace and makes direct coupling easy to take into account. For resonances with Q's of order 10^6, the fitting routine resolves f_0 and f_B to better than 1 Hz. Even at low Q and in the presence of substantial direct coupling, Eq. 2.6 models the data extremely well, only breaking down for samples with nonlinear absorption such as superconductors with weak links.

The microwave circuit used in the experiment is shown in Fig. 2.6. The 8722ES is connected directly to the input coaxial line and provides input power levels up to -5 dBm.

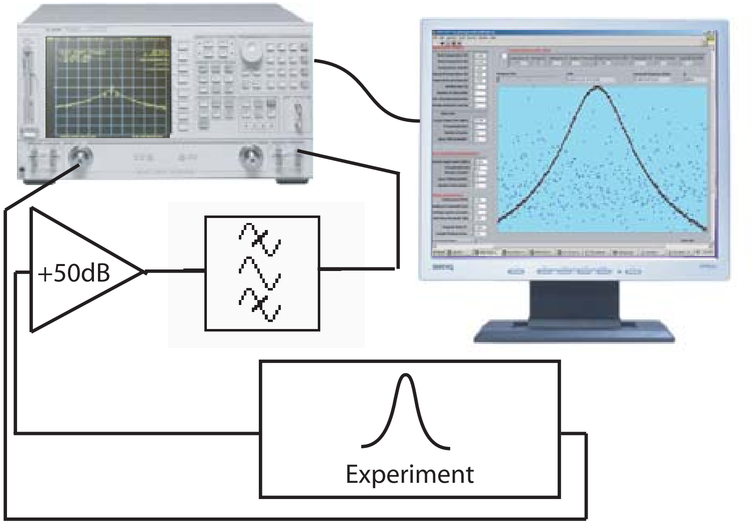

Figure 2.6: The measurements system used is

Several techniques are used to boost detection sensitivity, starting with the bandwidth-narrowing options built into the VNA. The 8722ES has Option 012, direct sampler access, allowing the 16 dB insertion loss of the VNA's input directional coupler to be bypassed. In addition, a peculiarity of the VNA's superheterodyne receiver allows substantial gains to be made by judicious preamplification. The receiver's local oscillator is a high order ($n \approx 200$) harmonic comb, which brings in noise at all the mixer's many image frequencies. Preamplification is carried out with a pair of Miteq AFS5 series amplifiers, each with $\approx$ 25 dB gain from 2 to 20 GHz and a noise figure (NF) $\approx$ 5 dB. These are followed by an HP8445B tunable YIG preselector (an Yttrium iron garnet resonator acting as a bandpass filter), with insertion loss (IL) $\approx$ 5 dB, that restricts the preamplifier gain to a 75 MHz band around the resonator frequency. This greatly reduces the noise at the mixer's image frequencies. Below 10 GHz, preamplification boosts the dynamic range of the VNA by close to the theoretical maximum of (Gain - NF - IL) $\approx$ 40 dB, tailing off at higher frequencies. At the low frequency end, the combination of direct sampler access and band-limited preamplification reduces the noise floor of the VNA to -165 dBm/Hz. This allows for operation with low input power, or for making low-noise measurements on very lossy samples without having to increase coupling.

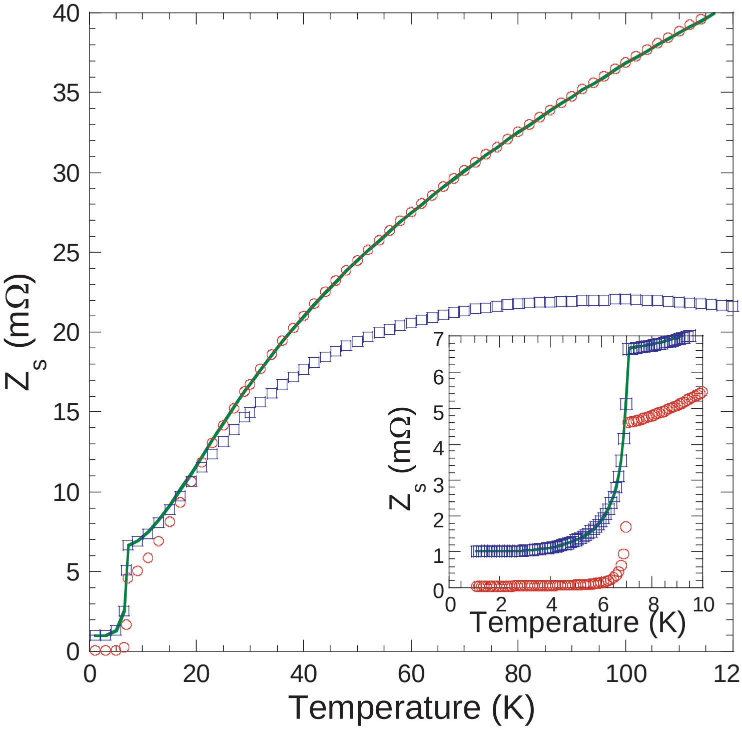

Figure 2.7: 5.49 GHz surface impedance data taken on a 350 μm diameter sphere of PbSn alloy. Open circles are the surface resistance, open squares are the measured surface reactance signal. A thermal expansion correction is applied to obtain the solid line, as explained in the text. Once corrected, the temperature dependence of R_s and X_s track accurately, allowing the *absolute* reactance to be obtained by matching R_s and X_s in the normal state. Inset: a close-up view of the surface impedance in the superconducting state, showing the weak temperature dependence expected at low temperature.

2.2.5 Calibration Measurements

In this section calibration measurements taken on a Pb reference sample are discussed. Fig. 2.7 shows 5.49 GHz surface impedance data for a calibration sample, a small sphere of PbSn alloy. By comparing the measured f_B data to the d.c. resistivity of the PbSn alloy the resonator constant Γ can be empirically determined to an accuracy of 2.5%. For a metal in the low frequency limit, R_s and X_s are expected to be equal in the normal state. Indeed, this is often the best way to set the origin in X_s, as it cannot be measured directly. However, the data in Fig. 2.7 reveal a large discrepancy. The disagreement is due to thermal expansion of PbSn, which contributes a significant error term ΔX_s^{th} to the surface reactance. Thermal expansion has the same effect on the reactance as a decrease in the penetration depth, so

$$\Delta X_s^{\mathrm{th}}(T) = -\omega\mu_0 \Delta r(T) = -\omega\mu_0 r \frac{\Delta\ell(T)}{\ell}. \tag{2.7}$$

For one spherical sample accurate dimensions were obtained by weighing with a microgram balance. From the mass, 254 ± 1 μg, the radius was computed as $r = 174.9 \pm 0.2$ μm. Using thermal expansion data from the literature[15], a correction term $-\Delta X_s^{\mathrm{th}}(T)$ was generated and added to the measured reactance signal. The corrected ΔX_s data are shown as the solid line in Fig. 2.7. Note that there are no free parameters in this analysis. The temperature dependence of the corrected X_s data tracks $R_s(T)$ very accurately above 25 K, allowing the *absolute* reactance to be determined by matching R_s and X_s in that temperature range. It should be pointed out that the thermal expansivity of Pb is one of the largest of all elements. The thermal expansivities of oxides and transition metals such as Nb are typically over an order of magnitude smaller[15]. Nevertheless, it is always necessary to rule out thermal expansion as a potential source of error in a measurement of the surface reactance.

Below 25 K, R_s and X_s deviate: this is a result of the increasing mean free path, which introduces relaxation and nonlocal effects into the surface impedance. The superconducting surface impedance is enlarged in the inset of Fig. 2.7, showing the exponentially flat temperature dependence of R_s and X_s at low temperatures, typical on an s-wave order parameter.

Chapter 3

The Chemistry of $YBa_2Cu_3O_{6+x}$

$YBa_2Cu_3O_{6+x}$ is unique among the cuprate superconductors in that it can be grown in single crystal form with cation disorder less than one part in 10^{-4} [38]. This allows for the study of the intrinsic physics of the superconducting state rather than what is often seen, the effects of defects in the crystal. $YBa_2Cu_3O_{6+x}$ is also unique in that the oxygen content, which controls the doping level, can be varied throughout the entire phase diagram through high temperature annealing[31, 38]. In high quality samples of this material the loosely held dopant oxygen atoms in the CuO-chain layers remain mobile at room temperature. In the weeks after the average oxygen content is set and homogenized, gradual ordering at room temperature into CuO-chain structures pulls electrons from the CuO_2 planes, smoothly increasing hole dopings over time[59, 54].

3.1 Crystal Structure and Oxygen Ordering

The crystal structure of fully oxygenated $YBa_2Cu_3O_7$ is shown in Fig. 3.1. With this oxygen content the sample would be superconducting with a T_c near 90 K. Optimal doping occurs at an oxygen content of 6.95 giving rise a T_c of about 93.5 K. YBCO has two CuO_2 planes per unit cell and one CuO chain. The doping of holes is mediated by oxygen atoms in the CuO chain layer.

The manner in which holes are doped into the CuO_2 planes is illustrated in Fig. 3.2. Copper atoms in an empty CuO chain layer are in the Cu^{1+} state. A neutral oxygen atom that enters the crystal will locate itself in the CuO chain layer and ionize two neighbouring copper atoms within the layer producing Cu^{2+} from Cu^{1+} leaving the oxygen atom in the

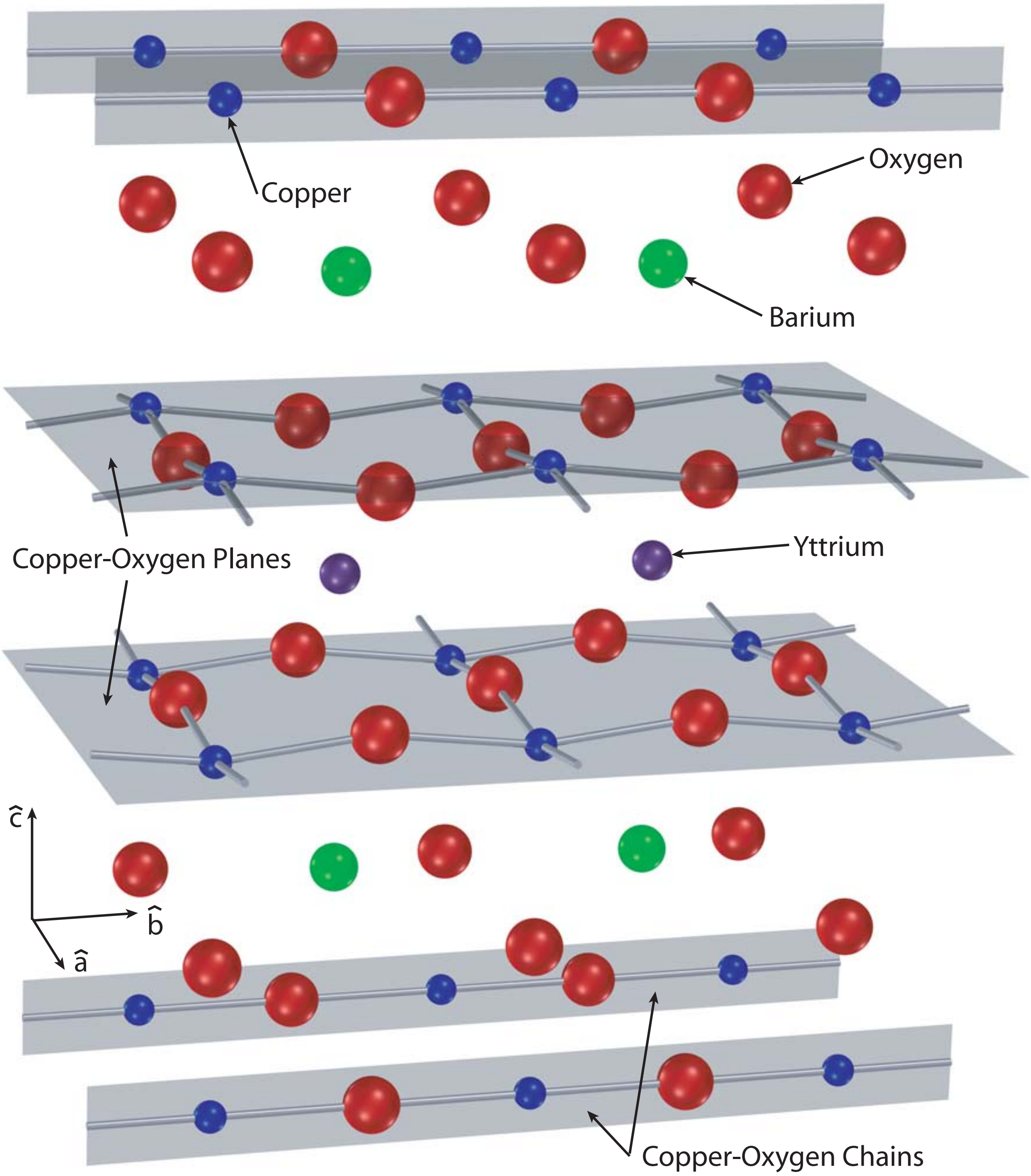

Figure 3.1: The crystal structure of fully oxygenated $YBa_2Cu_3O_7$.

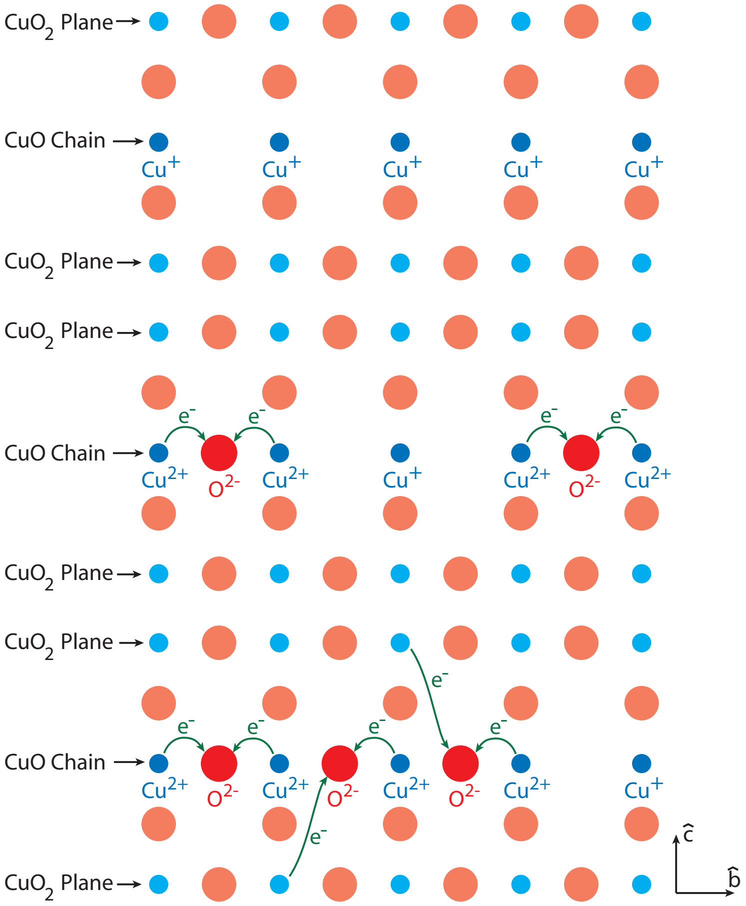

Figure 3.2: Oxygen ordering leads to doping of holes into the CuO_2 planes. The top CuO chain is empty so all the copper atoms are in the Cu^{1+} state. Adding oxygen to the chain layer oxidizes copper into the Cu^{2+} state. If oxygen atoms occupy neighbouring sites in the chain layer, a copper atom in the CuO_2 plane will be oxidized, leaving a hole in the plane.

O^{2-} state. If a second oxygen atom enters the layer at a position in the crystal well away from another oxygen atom, it will also oxidize two neighbouring copper atoms. If however, the oxygen atom enters a site immediately adjacent to another oxygen atom it will only have one neighbouring copper atom within the chain layer to oxidize, and thus will also oxidize a copper atom in a neighbouring CuO_2 plane. This leaves a hole in the CuO_2 plane. As the chains of oxygen atoms grow longer and longer, the hole doping is increased.

If the temperature of a $YBa_2Cu_3O_{6.333}$ sample is above 150 °C, oxygen atoms in the chain layer will be randomly dispersed along both the $\hat{a}$- and $\hat{b}$-axis, in what is known as the tetragonal phase[59, 54]. As the temperature drops below 150 °C the oxygen atoms will

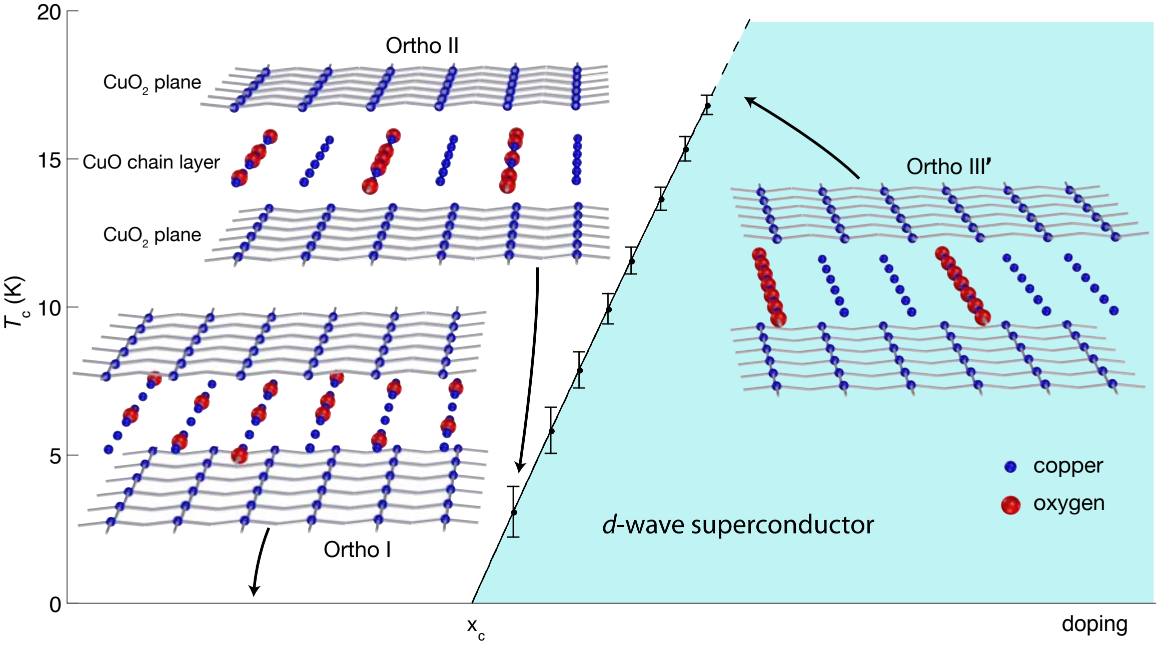

Figure 3.3: Illustration of oxygen ordering in the CuO chain layers of $YBa_2Cu_3O_{6.333}$. For $T \gg 150$ °C the material is tetragonal and oxygen atoms occupy *a*- and *b*-axis sites with equal likelihood (not shown). Below $T \approx 150$ °C the material adopts the Ortho-I structure, with oxygen randomly distributed amongst *b*-axis sites. Hole doping is very low in this phase and T_c=0. On annealing at room temperature for 3 to 6 weeks, the oxygen orders into the Ortho-II structure, with every second chain empty. Chainlets lengthen, introducing holes and making T_c small but finite. High hydrostatic pressure ($p \approx 20$ kbar) promotes further ordering at room temperature into the Ortho-III′ phase. T_c saturates at its maximum value for pressures greater than 14 kbar and the transition width ΔT_c, indicated by error bars, narrows markedly with increasing doping.

all enter $\hat{b}$-axis positions, a configuration known as the Ortho-I phase (shown in Fig. 3.3). At this point the sample is nonsuperconducting. If the sample is allowed to sit at room temperature, it will enter into the Ortho-II phase (also shown in Fig. 3.3), where every second chain is empty. At this point the sample will have a T_c of 1 to 2 K. In order to increase T_c further, pressure must be applied to the sample.

By placing the sample in a pressure cell at 20 kBar for a period of weeks, the oxygen can be encouraged to enter into the Ortho-III′ phase where every third chain is full, while the other two are empty. If the sample is then kept below about -10°C at ambient pressure it will stay in the Ortho-III′ phase.

3.2 Sample Preparation

Experimenters face multiple challenges measuring the microwave surface impedance of underdoped $\mathrm{YBa_2Cu_3O_{6+x}}$. Electronic anisotropy is greatly enhanced in these low doped samples[31], with the ratio of the c-axis to in-plane penetration depths λ_c/λ_{ab} approaching 100. As a result, measurements of ρ_s can only be carried out in special geometries that drive purely ab-plane currents, such as the small single-crystal ellipsoid used in this work.

Extremely pure single crystals of $\mathrm{YBa_2Cu_3O_{6+x}}$[37] were grown in barium zirconate crucibles and have cation disorder at the 10^{-4} level. For these experiments a crystal 0.3 mm thick was cut and polished with $\mathrm{Al_2O_3}$ abrasive into an ellipsoid with an average diameter of 0.35 mm. The oxygen content of the ellipsoid was adjusted to $\mathrm{O_{6.333}}$ by annealing at 914°C in flowing oxygen, followed by a homogenization anneal in a sealed quartz ampoule at 570°C and a quench to 0°C. At this point the sample was nonsuperconducting. After allowing chain oxygen order to develop at room temperature for three weeks, T_c was measured to be 3 K. The sample was then further annealed at room temperature for six weeks under a hydrostatic pressure of 14 kbar, raising T_c to 17 K. The sample was cooled to 0°C before removal from the pressure cell, and then stored at −10°C to prevent the oxygen order from relaxing. All further manipulation of the ellipsoid was carried out in a refrigerated glove box at temperatures less than −5°C. Periods of controlled oxygen disordering at room temperature and ambient pressure were used to generate a sequence of dopings as T_c relaxed back to 3 K. Subsequent reannealing under hydrostatic pressure of 23 kbar for a further six weeks returned T_c to the starting value of 17 K.

Chapter 4

Superfluid Density

The doping dependence of the temperature dependent superfluid density ρ_s has been obtained from a series of microwave surface impedance measurements, carried out at closely spaced doping intervals. As the normal contribution to the imaginary part of the conductivity is quite small, ρ_s is proportional to the imaginary part of the complex conductivity, which can be obtained from the surface impedance using the local-limit expression.

The superfluid density and its temperature dependance are fundamental properties of a superconductor. ρ_s determines the phase stiffness (the resistance of the superconducting order parameter to fluctuations in its phase) and its temperature dependance provides a direct probe of the current carried by quasiparticle excitations. The temperature dependance is entirely due to the form of the superconducting gap function, and thus serves as an indicator of the pairing symmetry, while the behaviour near the critical temperature reflects the importance of critical fluctuations.

4.1 Surface Impedance

The temperature dependance of the resonant frequency f_0 and half-power bandwidth f_B of the $\mathrm{TE}_{01(1-\delta)}$ mode of the rutile dielectric resonator were measured and related to surface impedance Z_s using the cavity perturbation formula (Eq. 2.2). The resonator constant was determined empirically using a Pb reference sample with similar dimensions to the $\mathrm{YBa_2Cu_3O_{6.333}}$ ellipsoid. This was accomplished by comparing the slopes of the d.c. resistivity and f_B^2 as functions of temperature. This procedure accounts for sample-to-sample variations in residual resistivity since $f_B^2 \propto R_s^2 \propto \rho_{dc}$. The sample was positioned at the

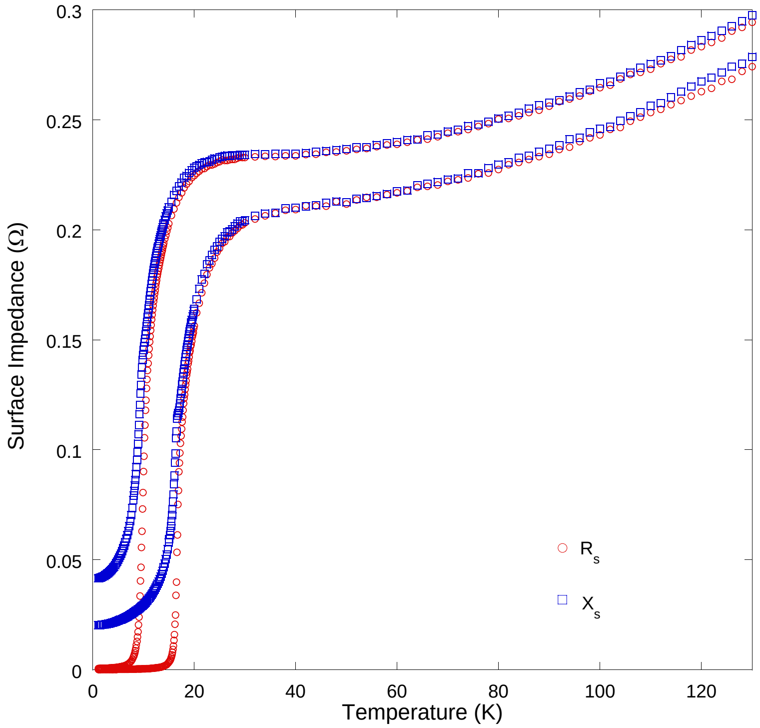

Figure 4.1: 5.48 GHz ab-plane surface impedance of an $\mathrm{YBa_2Cu_3O_{6.333}}$ ellipsoid, at dopings with T_c's of 16.8 K and 10.0 K. $R_s(T)$ is measured directly in the experiment, while the absolute reactance is obtained by offsetting $\Delta X_s(T)$ to match R_s and X_s in the normal state. The deviations evident at high temperatures is likely due to thermal expansion of the sapphire sample holder.

H-field antinode of the $\mathrm{TE}_{01(1-\delta)}$ resonator mode with the crystal's c-axis oriented along the microwave H field so as to induce purely ab-plane currents. Final alignment was carried out using magnetic torque in a 7 T field resulting in an alignment uncertainty of less than 1°. Once aligned the sample was kept in place for the duration of the doping study.

The surface resistance is determined by first subtracting the background half-power bandwidth measured when the sample is retracted from the resonator volume. The absolute surface reactance is then set by matching R_s and X_s in the normal state, where the imaginary part of the microwave conductivity is expected to be very small. Figure 4.1 illustrates this process for two of the hole dopings. The discrepancy at high temperatures is likely due to thermal expansion of the sapphire sample holder and is not corrected for as I am primarily concerned with low temperature properties where thermal expansion effects are negligible.

The low temperature surface impedance for all nine measured hole dopings is shown

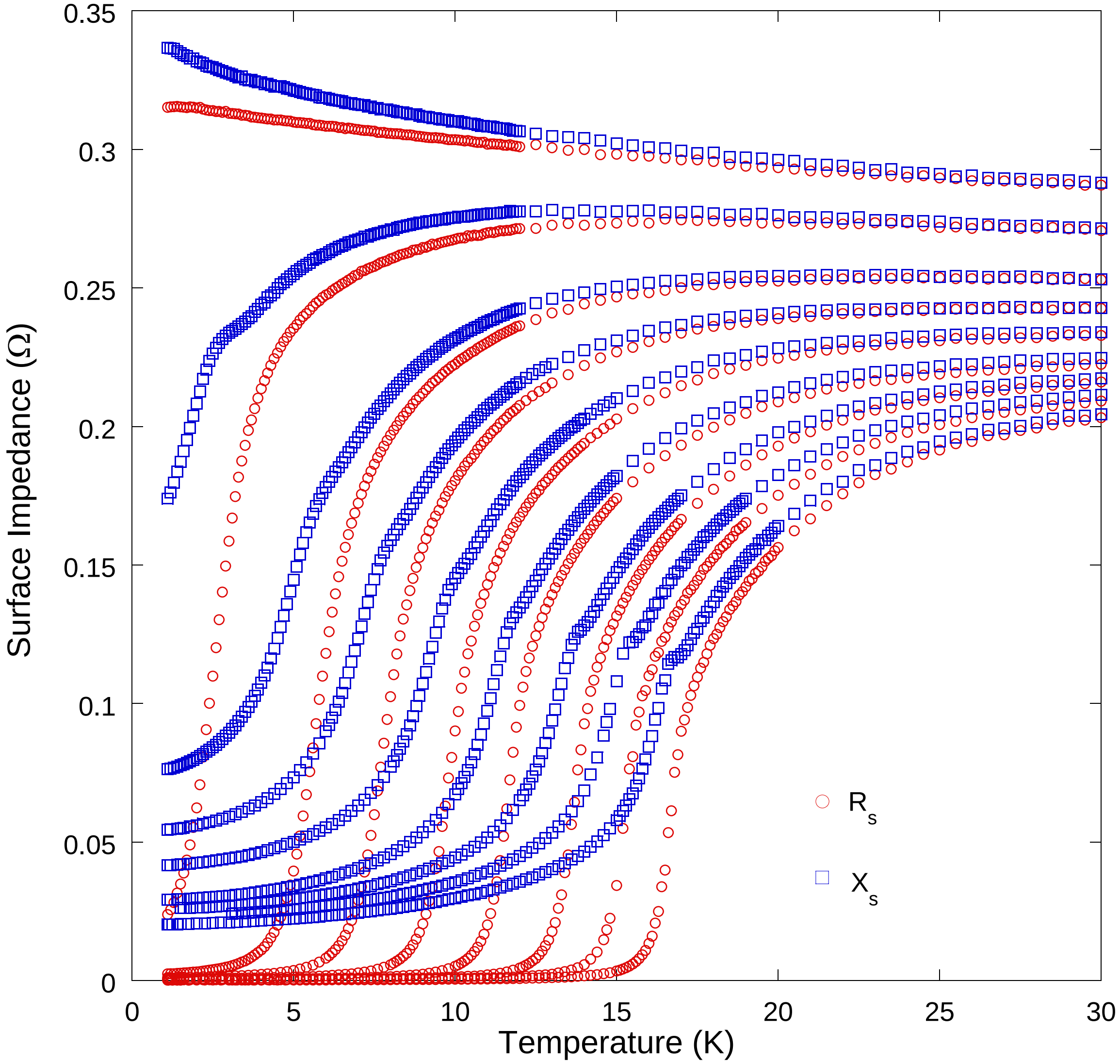

Figure 4.2: 5.48 GHz *ab*-plane surface impedance of an $YBa_2Cu_3O_{6.333}$ ellipsoid, at nine different dopings. $R_s(T)$ is measured directly in the experiment, while the absolute reactance is obtained by offsetting $\Delta X_s(T)$ to match R_s and X_s in the normal state. The apparent broadness of the transitions is due to fluctuations, not inhomogeneity of T_c.

in Fig. 4.2. The rounding of the transitions is due to superconducting fluctuations, not inhomogeneity of T_c as explained in Section 4.2. The small kink in X_s near T_c is believed to be due to the kinetic energy involved in accelerating the superfluid.

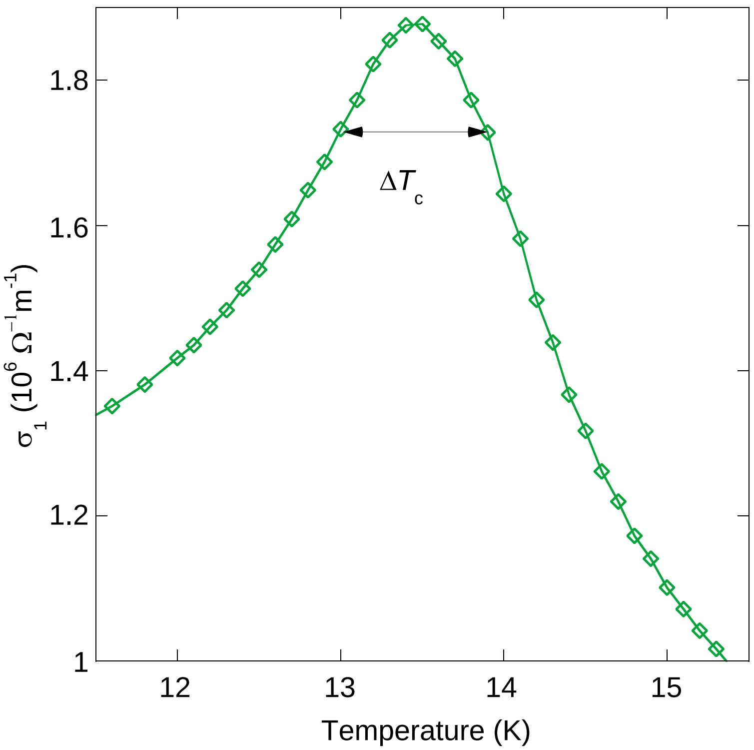

Figure 4.3: Real part of the conductivity $\sigma_1(T)$ obtained from the one of the surface impedance data sets shown in Fig. 4.2, showing a sharp fluctuation peak at T_c. ΔT_c is set to the difference between the inflection points in $\sigma_1(T)$ on opposite sides of the transition.

4.2 Conductivity

The complex microwave conductivity $\sigma = \sigma_1 - \mathrm{i}\sigma_2$ is obtained from the surface impedance data using the local-limit expression (Eq. 1.4). Figure 4.3 shows the sharp fluctuation peak in $\sigma_1(T)$ at 13.5 K for the the third highest doping. In the scaling theory of the superconducting transition[20], $\sigma_1(T)$ is expected to have upward curvature throughout the fluctuation region, with a sharp cusp at T_c. In real samples there is rounding of the fluctuation peak, and the estimated spread in T_c is found by equating ΔT_c to the difference in the inflection-point temperatures of $\sigma_1(T)$ on opposite sides of the transition. The doping dependance of ΔT_c is shown by the error bars in Fig. 3.3, which decreases in absolute size with increasing oxygen order. Given the steepness of $T_c(x)$ in this doping range the narrow transitions imply that the samples are highly homogenous on macroscopic scales. The real part of the conductivity σ_1 will be discussed in more detail in Chapter 5.

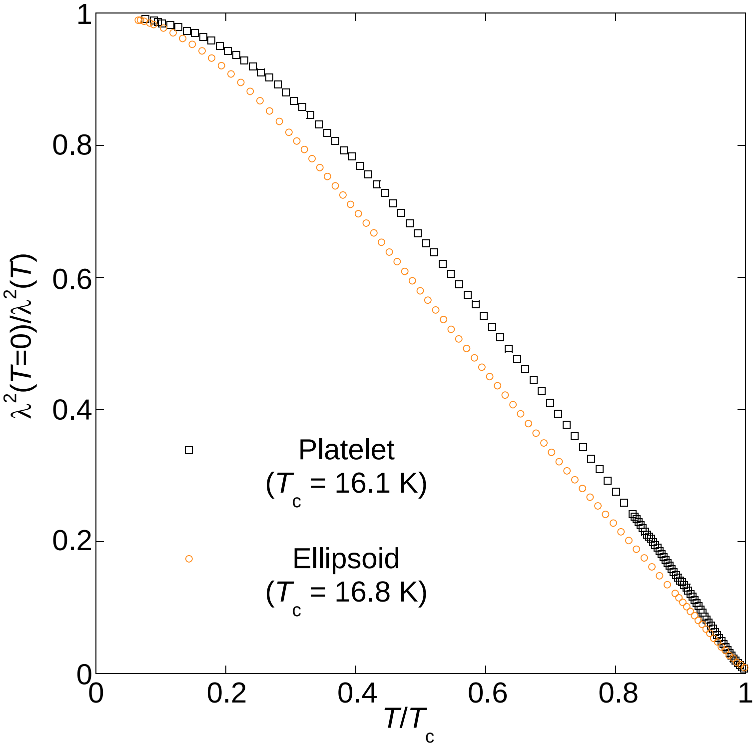

Figure 4.4: Sample dependence of the low temperature curvature in $1/\lambda^2(T)$. Data on a large platelet single crystal, measured using surface cavity perturbation, show substantially more curvature in $1/\lambda^2(T)$ than data from the ellipsoidal sample at comparable T_c.

4.3 Strong Scattering Effects

Strong scattering defects are present to some extent in all cuprate samples, and are known to drive a crossover from linear to quadratic behaviour in $\rho_s(T)$ below a cross-over temperature $T^* \approx \sqrt{\hbar\Gamma_N\Delta}/k_B$, where Γ_N is the normal state elastic scattering rate and Δ is the superconducting gap maximum[29, 30]. Bonn *et al.* examined the role of impurities in $YBa_2Cu_3O_{6+x}$ by making a systematic study of the effect of Zn and Ni dopants on $\lambda(T)$[11], confirming that the introduction of strong scatterers indeed changed the low temperature behaviour from a linear to a quadratic temperature dependence.

The effects of pair breaking are expected to become more prominent as T_c decreases in underdoped materials. Nevertheless, our $\rho_s(T)$ data reveal a wide range of linear temperature dependance, as seen in Fig. 4.4, with a sample-dependant T^* between 3 and 6 K. This suggests the origin of the low temperature curvature is extrinsic; that is, the curvature is

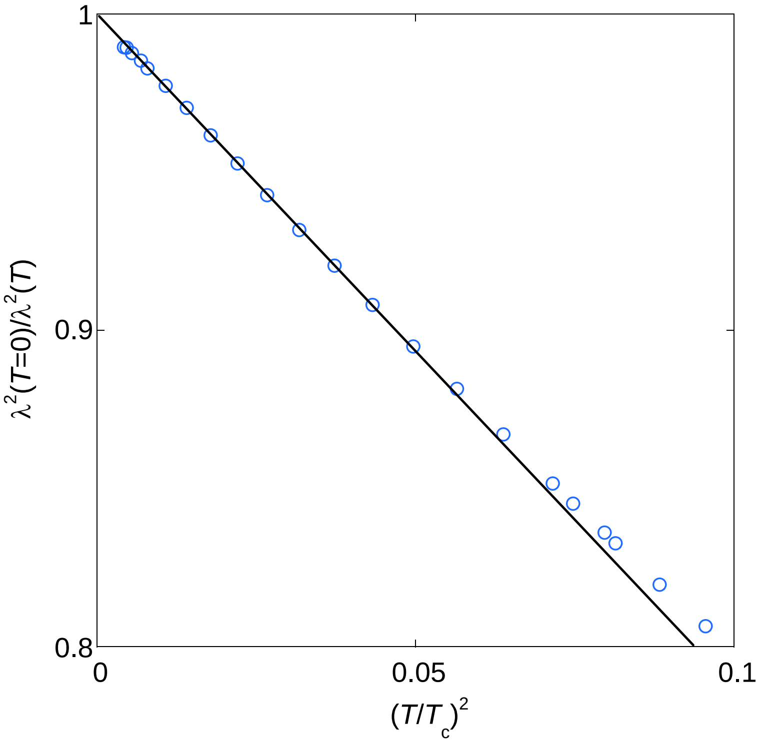

Figure 4.5: $\rho_s(T)$ vs. T^2, for the T_c=17 K data set. It shows that the asymptotic low temperature behaviour is quadratic, consistent with the effects of strong-scattering disorder.

not a property of the pure system. Also shown in Fig. 4.4 is $\rho_s(T)$ taken from surface cavity perturbation measurements by Dr. D. Broun on a large platelet crystal with a similar value of T_c. The ellipsoid appears to be considerably cleaner, with the linear regime of $\rho_s(T)$ extending to lower temperatures. The low temperature behaviour of $\rho_s(T)$, shown in Fig. 4.5, is accurately quadratic, consistent with the strong-scattering theory[11, 29, 30]. Oxygen disorder is unlikely to be the source of pair-breaking, as it is located out of the CuO_2 planes and T^* shows little change with increasing ordering of the CuO chains as seen in Fig. 4.6. There is, however, a difference in the temperature dependance of the superfluid density for samples with T_c's above and below about 11 K. This is shown most dramatically in a plot of $\lambda^2(T=0)/\lambda^2(T)$ versus T/T_c as discussed in Sec. 4.7.

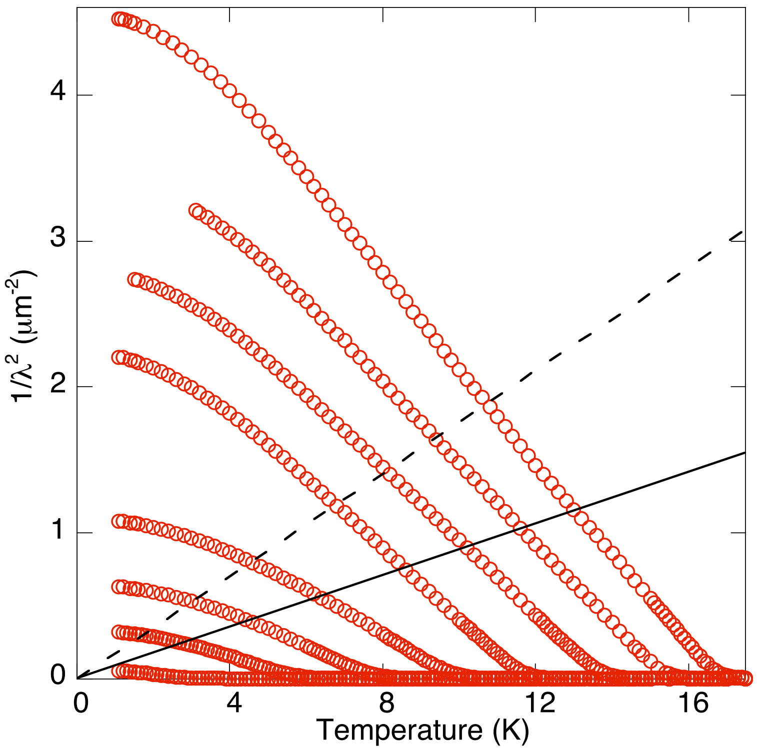

Figure 4.6: Doping dependance of the superfluid density. $\rho_s(T)$ of an $YBa_2Cu_3O_{6.333}$ ellipsoid, measured starting in the most ordered state (T_c=17 K) followed by controlled oxygen disordering in small steps down to T_c=3 K. Lines mark where the vortex-unbinding transition should occur for a 2-D superconductor. The dashed line corresponds to $\rho_s = (8e^2\mu_0 k_B/\pi\hbar^2 d)T$ in each CuO_2 plane. The solid line shows $\rho_s = (8e^2\mu_0 k_B/\pi\hbar^2 d)T$ in each CuO_2 bilayer.

4.4 Lack of a Kosterlitz-Thouless-Berezinski Transition

The temperature dependant superfluid density $\rho_s(T)$ is given by

$$\rho_s(T) \equiv 1/\lambda^2(T) \approx \omega\mu_0\sigma_2(T). \tag{4.1}$$

Figure 4.6 shows $\rho_s(T)$ plotted as $1/\lambda^2(T)$ for all eight superconducting dopings. The most striking feature of the data at the highest dopings is the wide range of linear temperature dependance, extending from T_c down to $T \approx 4$ K. This is especially surprising, because underdoped $YBa_2Cu_3O_{6+x}$ has a highly anisotropic electronic structure[31], with $\lambda_c^2(T \to 0)/\lambda_a b^2(T \to 0) \approx 10^4$. As a result, superconducting phase fluctuations are expected to be two dimensional and should drive an abrupt Kosterlitz-Thouless-Berezinski

(KTB) vortex unbinding transition[34, 28].

The minimum 2D superfluid density at which a KTB transition is expected to occur is shown in Fig. 4.6 for both isolated CuO_2 planes and for bilayers as the dashed and solid lines respectively. For bilayers the phase stiffness is expected to be stronger so that T_KT is lower. $\rho_s(T)$ passes smoothly through both of these lines, with no indication of a vortex unbinding transition or even of 3D critical fluctuations. Recent work has shown that the KTB transition does occur in ultrathin $YBa_2Cu_3O_{6+x}$ films, but that the effective thickness for the fluctuations is the film thickness[61, 62]. This data supports the fact that the effective thickness is the film thickness and shows that in bulk samples the transition is mean-field like.

4.5 Temperature Slope of the Superfluid Density

A central issue in the underdoped cuprates is whether the low temperature superfluid density is controlled by quasiparticle excitations or phase fluctuations. Phase fluctuations, if present, are acting unconventionally, as there is no KTB transition. If instead quasiparticles play the dominant role, the low temperature superfluid response will be governed by excitations near the gap nodes. In that case

$$\rho_s(T) = \rho_{s0} - \frac{2\ln 2}{\pi}\frac{k_B}{\hbar^2}\frac{1}{d}\alpha^2\frac{v_F}{v_\Delta}T, \tag{4.2}$$

where $\frac{v_F}{v_\Delta}$ is the ratio of the quasiparticle group velocities perpendicular and parallel to the Fermi surface and α is the charge-current renormalization factor [36, 18]. $|\mathrm{d}\rho_s/\mathrm{d}T|$, which is proportional to $\alpha^2\frac{v_F}{v_\Delta}$, is plotted in Fig. 4.7. At low dopings the slope decreases approximately linearly with T_c. In this range v_F is known to vary only weakly with doping[60]. The decrease in $|\mathrm{d}\rho_s/\mathrm{d}T|$ is unlikely to be due to a divergence of v_Δ, so must be primarily due to α. Such behaviour can arise in several ways. Within the Fermi liquid framework, weak residual interactions between electrons lead to backflow currents, reducing the total electrical current carried by a quasiparticle [56, 43, 18, 34]. Alternatively, in some distinctly non-Fermi-liquid theories of the under-doped cuprates, such as the slave-boson gauge theories of Anderson's resonating valence bond model [8, 33, 36, 56], the superconducting quasiparticle is a combination of a chargeless spinon and a spinless holon, with an effective charge that shrinks to zero upon underdoping. U(1) and SU(2) gauge theories [33, 36, 56] predict $\alpha^2 \sim \rho_{s0}^2$, a result also obtained in theories of fluctuating d-wave superconductors

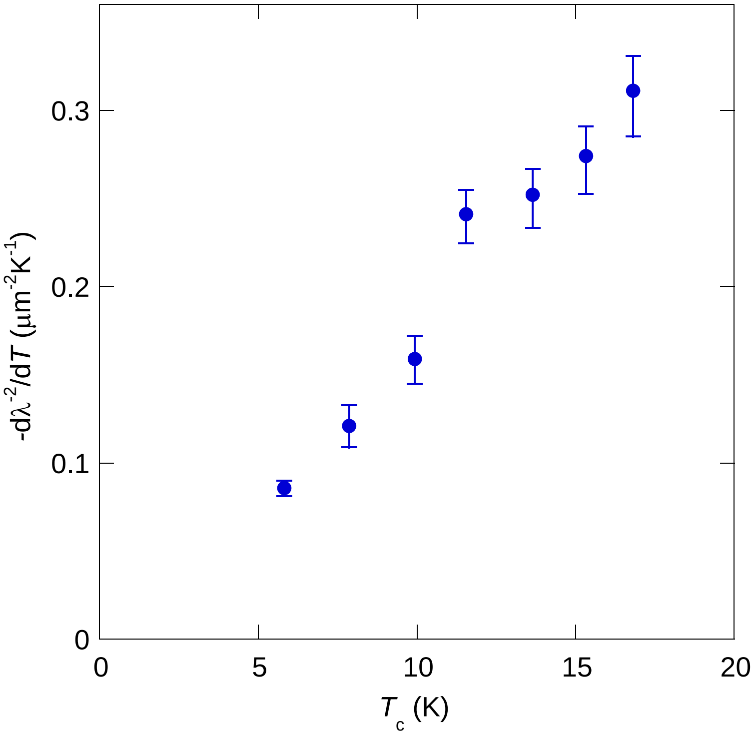

Figure 4.7: Temperature slope of the superfluid density. $|\mathrm{d}\rho_s(T)/\mathrm{d}T|$ is obtained from linear fits to $\rho_s(T)$ between 4 K and T_c. Error bars represent the combined uncertainties in calibration, matching of R_s and X_s, and sample alignment.

[23, 26, 27]. The observed doping dependence of α, however, is much weaker than predicted.

An alternative cause of the decline in $|\mathrm{d}\rho_s/\mathrm{d}T|$ is the onset of microscopic phase separation with underdoping, resulting in a gradual rescaling of $\rho_s(T)$ in proportion to the nonsuperconducting fraction. However, examination of the c-axis superfluid response indicates that this is unlikely. Figure 4.8 shows a plot of the normal fluid density for both in-plane and out-of-plane currents. The normal fluid density,

$$\rho_n(T) \equiv 1/\lambda^2(T \to 0) - 1/\lambda^2(T), \tag{4.3}$$

is sensitive to the energy spectrum of the nodal quasiparticles and directly probes their current response[49]. For in-plane currents, $\rho_n(T)$ fans out with doping, a consequence of the doping dependant slope. By contrast, for currents out of the plane, $\rho_n(T)$ collapses onto a single, doping independent curve away from T_c. This is consistent with a negligible doping dependence of v_F and v_Δ, and would not be the case if the superconducting volume

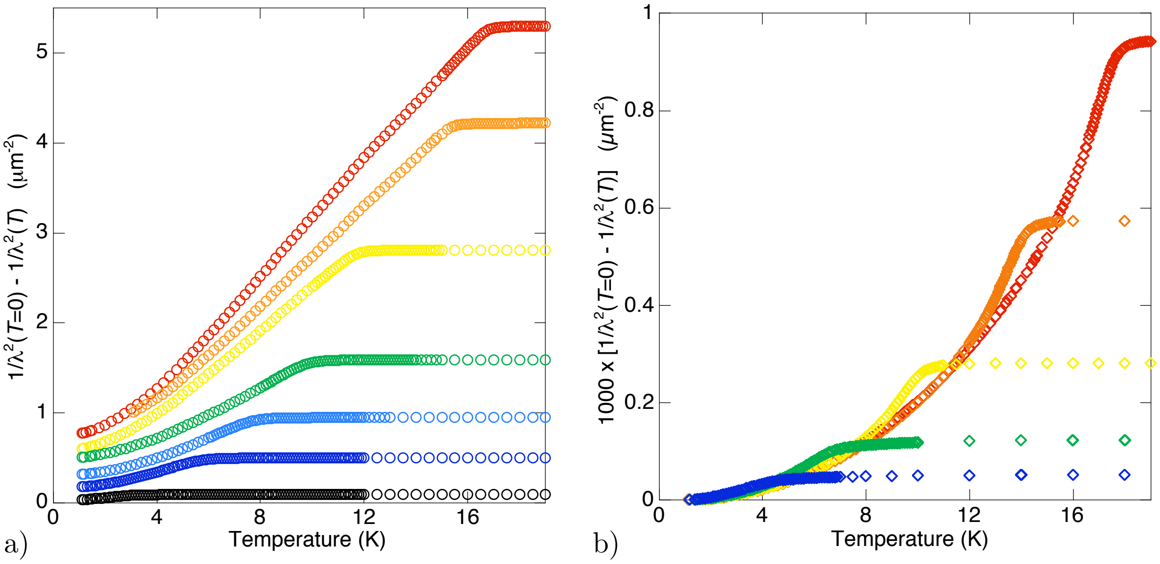

Figure 4.8: Anisotropy of the normal fluid density. $\rho_n \equiv 1/\lambda^2(T \to 0) - 1/\lambda^2(T)$ is a probe of the supercurrent carried by quasiparticle excitations close to the d-wave gap nodes, and is sensitive to the effects of charge-current renormalization. a) For currents *within* the CuO_2 planes, $\rho_n(T)$ fans out with doping, revealing a clear increase in temperature slope. b) For currents *perpendicular* to the CuO_2 planes, all the $\rho_n(T)$ data coalesce onto a common curve, independent of doping. This suggests that c-axis currents are *not* renormalized, and argues against microscopic phase separation as the cause of the unusual behaviour of the in-plane superfluid density. $\lambda_c(T)$ data are taken from Ref. [31]. For clarity not all data sets are shown.

fraction were shrinking on underdoping. Instead, the decline of $|\mathrm{d}\rho_s/\mathrm{d}T|$ is seen to be purely a property of the in-plane quasiparticles, indicating that they are very different from the physical electrons that tunnel between layers.

The anomalous behaviour of ρ_s revealed by these experiments has motivated new theoretical work. Herbut has shown that the problem of nodal quasiparticles coupled to strong phase fluctations maps onto the weakly interacting, anisotropic 3D Bose gas, due to the short-ranged nature of the Coulomb interaction in layered superconductors [27, 14]. In that model $\rho_s(T)$ should be given at low dopings by the condensate fraction of a noninteracting Bose gas, $\Delta\rho_s(T) \sim T\ln(T/t)$, with t the interlayer Josephson coupling. This correctly captures the linear T dependence of $\rho_s(T)$ and the lack of a critical region, but is at odds with the decline of $|\mathrm{d}\rho_s/\mathrm{d}T|$ as $T_c \to 0$. Franz and Iyengar have proposed an alternative theory based on vicinity to a quantum critical point, which they argue makes the relevant model of phase fluctuations a (3+1)D–XY model, leading naturally to a mean-field transition [21]. Within this framework they calculate the renormalization of of the zero temperature superfluid density ρ_{s0} and the effective quasiparticle charge, and find behaviour in qualitative accord with our experimental observations. We also point out that recent neutron scattering experiments on $\mathrm{YBa_2Cu_3O_{6+x}}$ with $T_c = 18$ K have revealed short-range, fluctuating spin correlations, but rule out phase separation and coexistence of superconductivity with long-range-ordered antiferromagnetism [52]. This raises the interesting possibility that the behaviour of ρ_s is linked to the emergence of intrinsic, bulk magnetism. Future experiments will aim to test this connection, but it seems suggestive that slowly fluctuating spin structures are observed at the point where $|\mathrm{d}\rho_s/\mathrm{d}T|$ develops a strong doping dependence.

4.6 Correlation Between T_c and ρ_{s0}

One of the longest standing results in the study of underdoped cuprate superconductors is that of a linear correlation between the transition temperature T_c and the zero temperature superfluid density ρ_{s0}. This strong correlation has led many to believe that it is the superfluid density that controls T_c in the underdoped cuprates[19, 26, 13]. As ρ_{s0} is the energy scale for fluctuations in the phase of the order parameter, it is postulated that above T_c superconductivity persists locally with long range phase coherence setting in at T_c.

My measurements show a sub-linear power law for the correlation between T_c and $\rho_{s0} \equiv 1/\lambda^2(T \to 0)$ as shown in Fig. 4.9. The dip seen at $\rho_{s0} = 2.5\ \mu\mathrm{m}^{-2}$ will be discussed in Section 4.7. Fig. 4.10 shows this data plotted on a logarithmic axis alongside existing data for single crystal and thin film $\mathrm{YBa_2Cu_3O_{6+x}}$. These include: very recent μSR data on single crystals[50]; data from $\mathrm{Gd^{3+}}$ ESR, taking the geometric mean of the a and b-axis values[47]; H_{c1} data, converted to superfluid density assuming the Ginzburg-Landau parameter $\kappa = 50$[40] and mutual inductance measurements on thin film $\mathrm{YBa_2Cu_3O_{6+x}}$[61]. The sublinear correlation persists to optimal doping, although the data cannot be described by a single power law. Scaling theory[35] predicts that $T_c \propto \rho_{s0}^y$ with $y = 1/2$ in the underdoped cuprates, where the system is close to a zero-temperature critical point so that it is three dimensional and quantum fluctuations are important. At this point most other theories predict a linear correlation in accord with the first measurements of ρ_{s0} in underdoped cuprates. The value $y = 1/2$ is very close to what is observed in my measurements and in a recent study[61] on thin film $\mathrm{YBa_2Cu_3O_{6+x}}$ that reports $T_c \propto \rho_{s0}^{0.43}$. It should also be noted

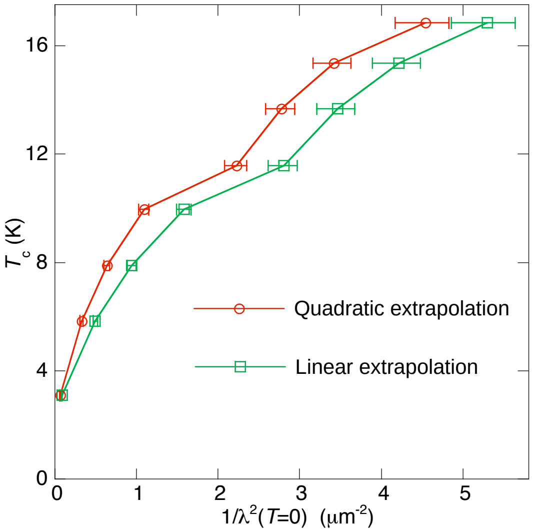

Figure 4.9: Correlation between T_c and the zero-temperature superfluid density. $\rho_{s0} \equiv 1/\lambda^2(T \to 0)$ is obtained by both linear and quadratic extrapolation to $T = 0$. The error bars indicate the combined uncertainties in calibration, the X_s offset, and sample alignment. The data reveal a clear sublinear correlation.

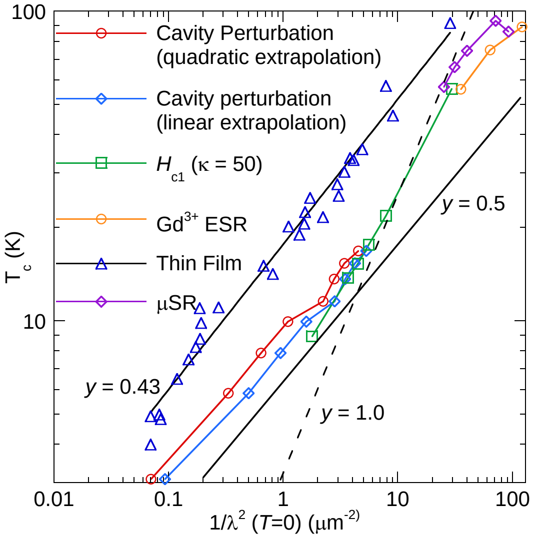

Figure 4.10: Correlation between T_c and the zero-temperature superfluid density shown on a log-log plot. Shown are data from: Gd^{3+} ESR, taking the mean of a and b-axis values [47]; lower critical field H_{c1} measurements, assuming $\kappa = 50$ [40]; μSR [50]; thin films[61]; and the cavity perturbation results reported in this work. Lines indicate different power laws, $T_c \propto \rho_s^n$. T_c decreases smoothly over more than 3 decades in the superfluid density, with a sublinear correlation extending over the whole range. The superfluid density in the thin films follows a similar power law but is nearly an order of magnitude lower in magnitude.

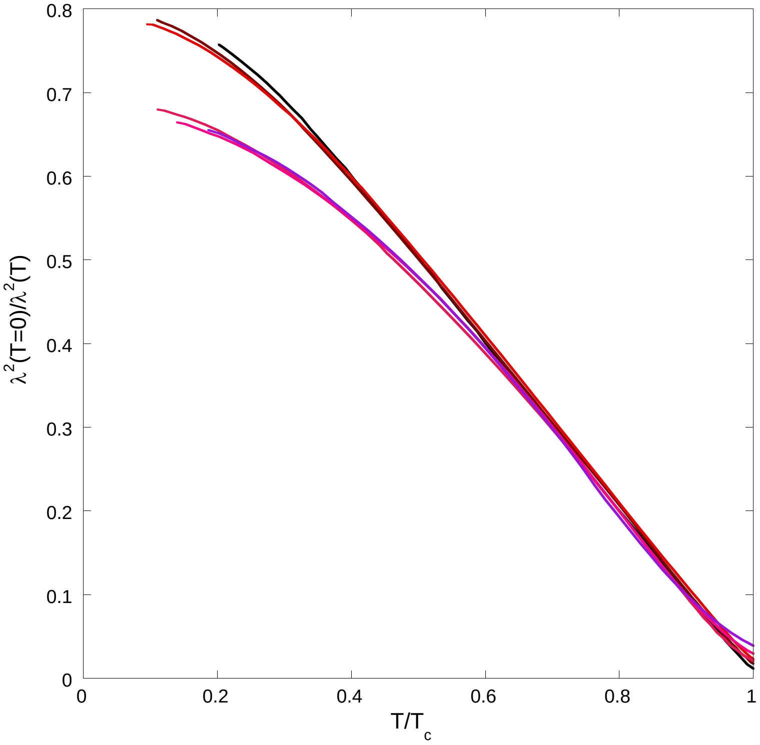

Figure 4.11: $\lambda^2(T=0)/\lambda^2(T)$ versus T/T_c. The superfluid density can be scaled by matching the slopes of the plots of $1/\lambda^2(T)$ just below T_c. The scaled superfluid density falls on two different curves for $T_c > 11$ K (the upper curves) and $T_c < 11$ K (the lower curves), presenting the possibility of a phase transition for a T_c around 11 K.

that the absolute values of ρ_{s0} at low dopings in the thin film measurements are almost an order of magnitude smaller than in single crystal $YBa_2Cu_3O_{6+x}$, due either to granularity or substantial pair breaking effects in the thin films. Despite the strong correlation between T_c and ρ_{s0}, the apparent lack of a universal correlation raises the possibility that phase fluctuations might not ultimately limit T_c in the underdoped cuprates.

4.7 Phase Transition?

Our measurements reveal a kink in the function $T_c(\rho_{s0})$ for a T_c of about 11 K, and a qualitative change in the temperature dependence of ρ_s at this doping. Figure 4.11 shows $\rho_s(T/T_c)$ scaled so that the slope of $\rho_s(T)$ is equal for all dopings just below T_c. For $T_c > 11$ K the scaled superfluid density falls onto the upper curve, with an abrupt transition to the lower temperature dependance for lower dopings. The abruptness of the change is shocking, suggesting a sudden switching on of extra pair breaking below some critical doping. One possibility is that this is connected to the onset of long-range magnetic order. Stock *et al.* have recently observed short-range, fluctuating spin correlations in neutron scattering experiments on $\mathrm{YBa_2Cu_3O_{6+x}}$ with T_c=18 K[52]. They rule out phase separation and coexistence of the superconductivity with long-range-ordered antiferromagnetism. The T_c at which the temperature dependance changes is below that of the sample studied by Stock *et al.*[52], so long-range magnetic ordering or phase separation could be causing the change seen in our data. A more detailed study of this region is planned.

Chapter 5

Microwave Conductivity

The same surface impedance data and electrodynamic analysis used to obtain $\rho_s(T,x)$ in the previous chapter yields the real part of the conductivity σ_1 associated with dissipative processes and electrical transport in the superconductor. The results of this analysis are shown in Fig. 5.1 where it can be seen that the conductivity increases upon entering the superconducting state for all dopings, while at low T it appears to decrease slightly. For the purposes of separating quasiparticles and fluctuations, it is clear at the highest dopings that we can interpolate through the fluctuation peak. In the superconducting state the number of charge carriers is decreasing with temperature as they pair up and condense into the superfluid so an increase in the conductivity must imply that the quasiparticle transport relaxation rate is decreasing more rapidly than the normal fluid fraction.

5.1 Two-Fluid Analysis

Additional information can be extracted using a two-fluid model of the conductivity. In a superconductor the superfluid condensate conducts in parallel with quasiparticle excitations. The superfluid conductivity is dissipationless and takes the form

$$\sigma_s(\omega) = \frac{n_s e^2}{m^*}\left(\pi\delta(\omega) + \frac{1}{\mathrm{i}\omega}\right). \tag{5.1}$$

The zero-frequency delta function represents the energy absorbed in accelerating the superfluid and is required by the conductivity sum rule. The conductivity sum rule,

$$\frac{1}{\pi}\int_{-\infty}^{\infty}\sigma_1(\omega)\mathrm{d}\omega = \frac{ne^2}{m}, \tag{5.2}$$

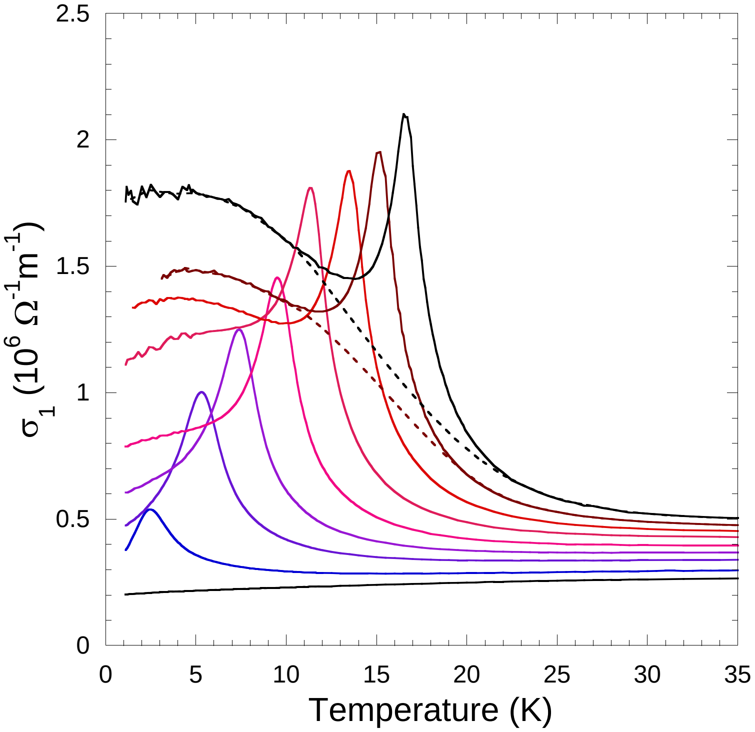

Figure 5.1: The real part of the conductivity $\sigma_1(T)$ obtained from the surface impedance data via Eq. 1.4. The dashed lines are a guide to the eye to indicate how the conductivity separates into fluctuation and quasiparticle components.

applies to all systems of electrons and states that the total area under the curve $\sigma_1(\omega)$ is constant. This is illustrated in Fig. 5.2 where in the normal state we have a Drude conductivity. Somewhat below T_c the scattering rate has decreased resulting in a much narrower spectrum with a zero-frequency delta function due to the superfluid condensate. The height of the spectrum has increased in order to keep the total area constant in agreement with the conductivity sum rule. At very low temperatures the delta function has grown and the loss of normal carriers has lowered the low frequency conductivity. All of the above situations can be described by the Drude two-fluid model of Equation 1.5.

Knowing the real and imaginary parts of the conductivity enables one to extract the scattering rate $1/\tau$ and normal fluid fraction f_n using the two-fluid model of Eq. 1.5. The equations used are shown below.

$$\omega\tau = \frac{\sigma_1(T)}{\sigma_2(0) - \sigma_2(T)} \tag{5.3}$$

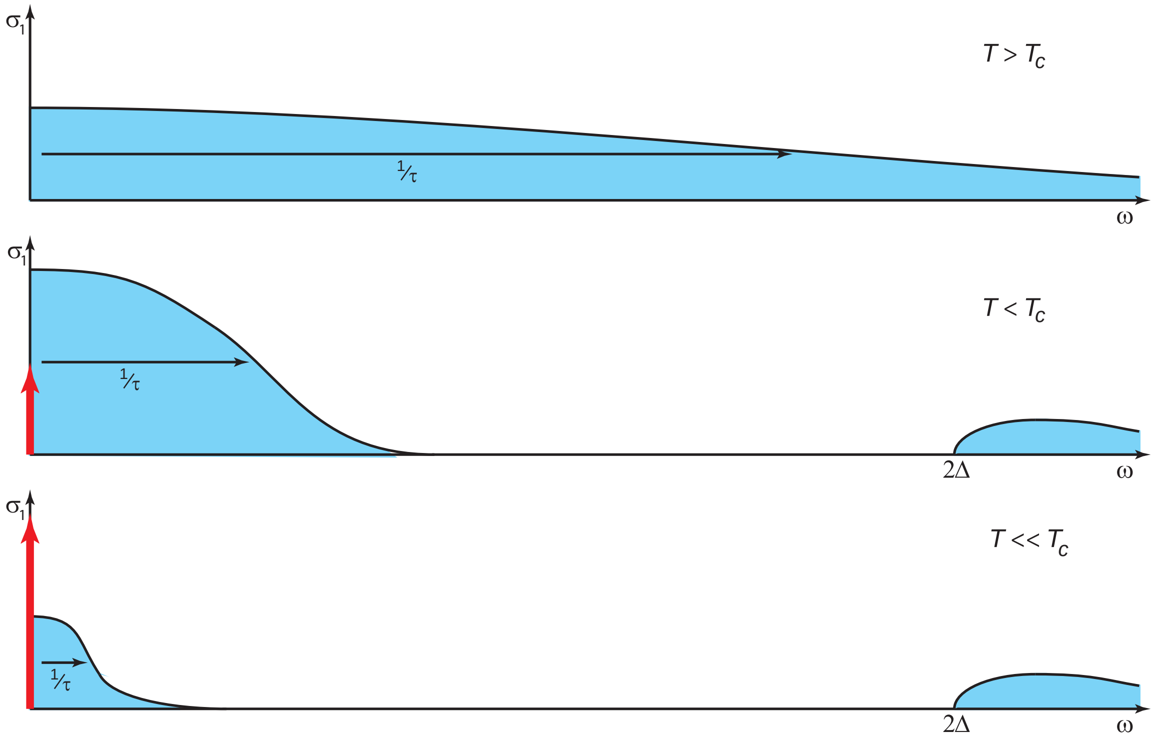

Figure 5.2: Quasiparticle conductivity spectrum at three different temperatures. The red arrow represents the zero-frequency delta function.

$$f_n = (1+\omega^2\tau^2)\frac{\sigma_2(0)-\sigma_2(T)}{\sigma_2(0)} \tag{5.4}$$

Here $\sigma_2(0)$ represents the total spectral weight as determined by a linear extrapolation of $\rho_s(T)$ to $T = 0$[55].

5.2 Normal Fluid Fraction

The normal fluid fraction f_n extracted from our data using Eq. 5.4 is shown in Fig. 5.3. The two-fluid analysis requires allowing for a residual f_n at $T = 0$ K. The natural way to determine this is by extrapolating the linear part of $\rho_s(T)$ to $T = 0$. The amount of residual normal fluid evident in Fig. 5.3 is supported by unpublished broadband microwave measurements performed by Dr. P. Turner and J. Bobowski. It can be noted that the relative normal fraction is decreasing with T_c, while the absolute value is increasing nearly linearly. Pair breaking, the cause of residual normal fluid, is complicated, and is related to

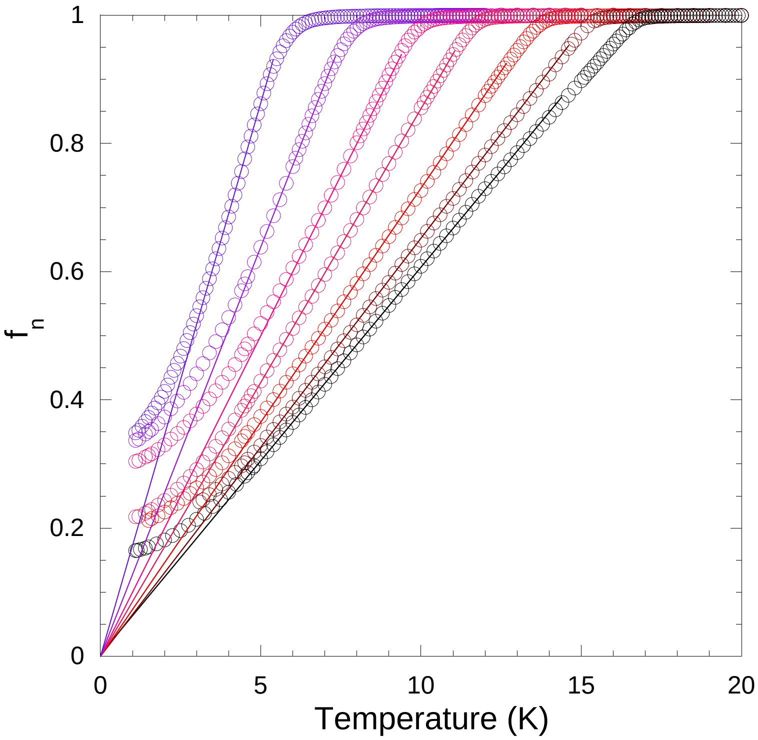

Figure 5.3: The normal fluid fraction f_n versus T. All data sets show a large linear regime.

the strong scattering effects described in Sec. 4.3.

5.3 Quasiparticle Transport Relaxation Rate

Equation 1.5 can be rearranged to extract the quasiparticle transport relaxation rate $1/\tau$ from the conductivity data with the result of such an analysis is shown in Eq. 5.3. The results are shown in Fig. 5.4. The dashed line illustrates how one can interpolate through the fluctuation peak to obtain the actual relaxation rate. Upon entering the superconducting state the relaxation rates drop dramatically with all of the data falling onto the same curve at low T. This behaviour suggests that the nodal spectrum, defined by

$$E_p = \sqrt{(v_F p_\perp)^2 + (v_\Delta p_\|)^2}, \tag{5.5}$$

where $p_\perp$ and $p_\|$ are the momentum perpendicular and parallel to the fermi surface, doesn't change in this doping range, consistent with the c-axis ρ_n data shown in Fig. 4.8b. This in turn suggests that density of states around the node is unchanged in this doping region.

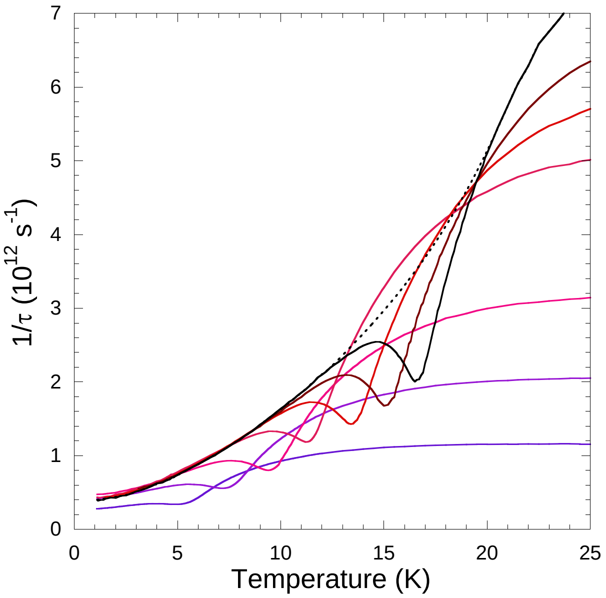

Figure 5.4: The quasiparticle scattering rate versus temperature for all dopings. The dashed line shows an interpolation through the fluctuation peak. At low T all of the scattering rates fall on the same curve except for the lowest doping.

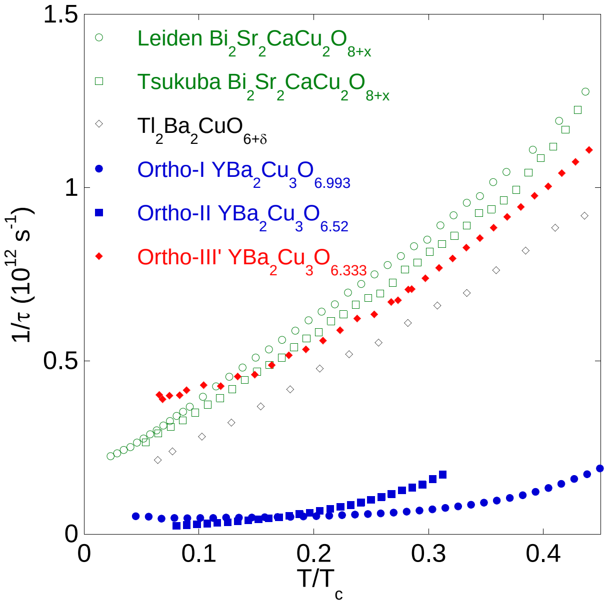

Figure 5.5: Quasiparticle scattering rate for six different samples. Although that Ortho-III′ $YBa_2Cu_3O_{6+x}$ has a much higher scattering rate than either Ortho-I or Ortho-II $YBa_2Cu_3O_{6+x}$, it is different than the other cuprates, saturating at low T while the others pass nearly linearly through $T = 0$. All other data taken from [46].

The relaxation rate shown in Fig. 5.4 is saturating at a low temperature value of 0.4×10^{12} s^{-1} which, converted into temperature units using $\hbar/\tau = k_B T$, is 3 K. This corresponds quite well with the scattering induced crossover temperature T_* in the superfluid density of 3 to 6 K. The mean free path can also be calculated if the Fermi velocity v_F is known. Zhou *et al.*[60] have shown that v_F is universal in the cuprates, with a value of 1.8 eV·Å. This is converted to SI units by dividing by $\hbar$, resulting in $v_F = 2.7 \times 10^5$ m/s. Assuming that quasiparticles are moving ballistically at this velocity we infer a mean free path $\ell = 0.7$ μm from our data.

A mean free path of 0.7 μm seems to move us out of the local limit as the penetration depth varies from about 0.43 μm to over 3 μm as the hole doping is decreased. However, the fact that data is consistent through out the entire doping regime suggests that the local limit is never lost. A possible explanation for this may have to do with differences between intranode and internode scattering.

In systems with extended scatterers intranode scattering occurs much more frequently than internode scattering events. Intranode scattering affects the group velocity of the quasiparticle but *not* the electrical current while internode scattering affects both so that from the point of view of electrical transport quasiparticles move diffusively rather than ballistically. The average distance moved between *strong* scattering events is then

$$\Delta x = \frac{\ell}{\sqrt{N}} \tag{5.6}$$

where N is the ratio of the single particle scattering rate Γ^{sp} to the transport scattering rate $\Gamma^{\rm tr}$,

$$N = \frac{\Gamma^{\rm sp}}{\Gamma^{\rm tr}} \tag{5.7}$$

which can be as high as 100[17]. Thus the quasiparticles would not move out of the penetration depth region between strong scattering events and the local limit would be upheld.

Figure 5.5 shows the transport relaxation rate for a number of different cuprate superconductors[46]. $\mathrm{YBa_2Cu_3O_{6+x}}$ usually has a very low relaxation rate as can be seen from the Ortho-I and Ortho-II data. This is due to the very low cation disorder as compared to $\mathrm{Bi_2Sr_2CaCu_2O_{8+\delta}}$ and $\mathrm{Tl_2Ba_2CuO_{6+\delta}}$. However, the underdoped sample that I have studied seems to have a transport relaxation rate more similar to $\mathrm{Bi_2Sr_2CaCu_2O_{8+\delta}}$ and $\mathrm{Tl_2Ba_2CuO_{6+\delta}}$ than to the other dopings of $\mathrm{YBa_2Cu_3O_{6+x}}$. This high scattering rate cannot by due to cation disorder as the cation disorder in $\mathrm{YBa_2Cu_3O_{6+x}}$ is independent of oxygen content. This leaves oxygen disorder as the one remaining candidate for chemical

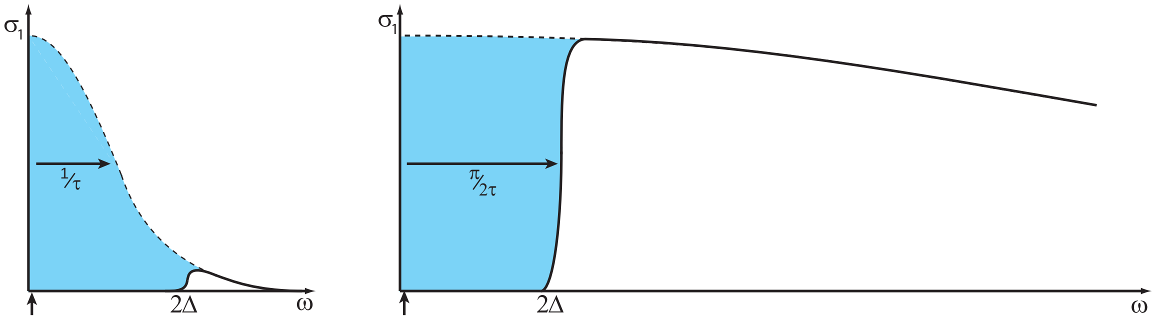

Figure 5.6: The conductivity spectral weight $\sigma_1(\omega)$ in the (a) clean limit and (b) dirty limit. The arrows indicate the approximate measurement frequency, while the shaded area represents the portion of the conductivity spectrum that collapses into the superconducting condensate.

disorder. However, we believe oxygen disorder to have a weak effect, because there is no systematic decrease in scattering as the Othro-III′ phase is approached. Why the relaxation rate is then so high is unknown. A possible explanation is that magnetic correlations gaining strength as the Mott insulating state is approached and these magnetic structures are scattering quasiparticles. Stock, Buyers, Yamani *et al.* have recently observed short-range, fluctuating spin correlations, but rule out phase separation and coexistence of the superconductivity with long-range-ordered antiferromagnetism in neutron scattering experiments on T_c=18 K $\mathrm{YBa_2Cu_3O_{6+x}}$[52].

Fig. 5.6 illustrates the differences in the conductivity spectrum $\sigma_1(\omega)$ for the clean and dirty limits. The arrows indicate the approximate measurement frequency. The dashed lines show the normal state spectrum. In the superconducting state a frequency corresponding to twice the gap energy is required to break pairs. In the clean limit nearly all of the spectral weight is condensed into the superfluid, while in the dirty limit only a small fraction of the spectral weight is condensed. The area of the shaded region is determined experimentally by the zero temperature superfluid density. Since my measurements were done at such a low frequency on the scale of the frequency spectrum, the normal state conductivity I have calculated determines the height of the conductivity spectrum. As a result the normal state relaxation rate determined by two-fluid analysis is the width of the shaded area as shown by $1/\tau$ in Fig. 5.6. Thus in the dirty limit, the normal state relaxation rate measures the size of the superconducting gap 2Δ, while in the clean limit it measures the width of the conductivity spectrum, i.e. the effective relaxation rate $1/\tau_{\mathrm{eff}} \sim \min(4\Delta/\pi, 1/\tau_{\mathrm{tr}})$.

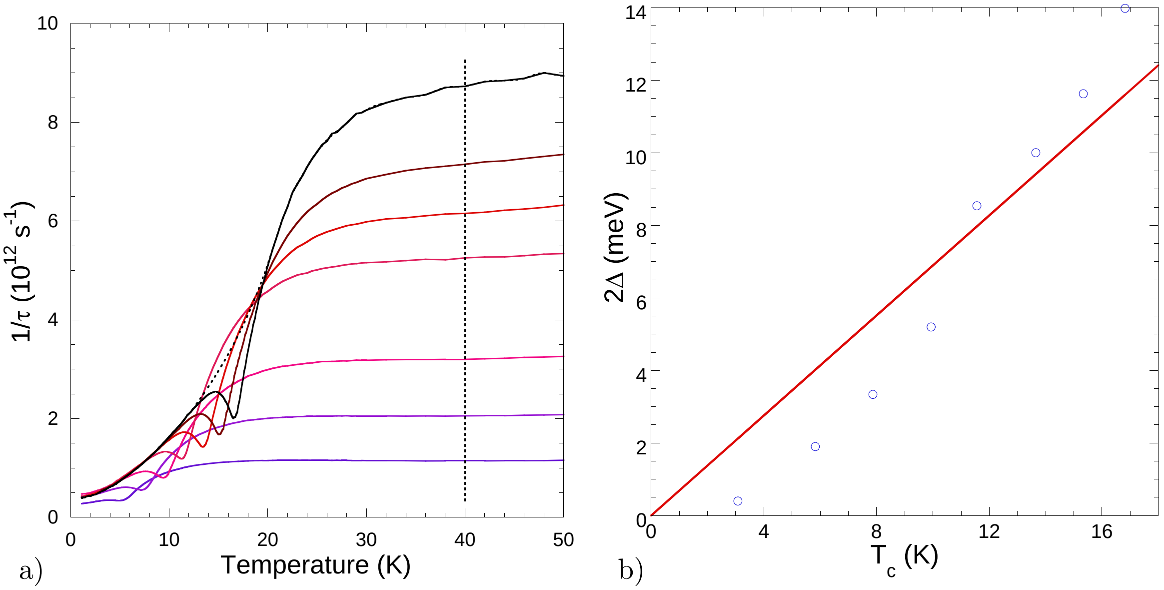

Figure 5.7: a) $1/\tau_{eff}$ versus T. The normal state relaxation rate is taken at $T = 40\ K$ which should correspond to 2Δ in the dirty limit. b) 2Δ versus T_c. The red line is $2\Delta = 8k_BT_c$. The gap energy appears to scale with T_c.

In the superconducting state $\mathrm{YBa_2Cu_3O_{6.333}}$ is in the clean limit and the effective scattering rate determined via the two-fluid analysis is the transport relaxation rate. However, in the normal state $\mathrm{YBa_2Cu_3O_{6.333}}$ is in the dirty limit as is evident in how the effective scattering rate shown in Fig. 5.7a approaches a constant value at higher temperatures. Thus, in the normal state, the effective scattering rate is related to the size of the superconducting gap. The size of the gap, 2Δ is plotted for the different hole dopings in Fig. 5.7. The red line is $2\Delta = 8k_BT_c$ which appears to correspond quite well with the data. This shows clear evidence for an increase in the size of the superconducting gap as a function of hole doping.

Chapter 6

Conclusion

Microwave cavity perturbation using new rutile dielectric resonators has allowed us to perform high resolution measurements of the surface impedance of highly underdoped $\mathrm{YBa_2Cu_3O_{6+x}}$. These measurements have provided unique insight into the physics of underdoped cuprate superconductors. The technique and the apparatus used in making these measurements is described in Chapter 2 of this thesis.

In Chapter 3 the chemistry of $\mathrm{YBa_2Cu_3O_{6+x}}$ is discussed, with an emphasis on the nature of the hole doping mechanism. The beauty of this mechanism is that it allows for a doping study to be performed on a single sample, with no change in oxygen content or cation disorder. This then allows us to study the intrinsic properties of $\mathrm{YBa_2Cu_3O_{6+x}}$, without being bothered by sample-to-sample variations, and in the future will lead to doping studies throughout the $\mathrm{YBa_2Cu_3O_{6+x}}$ phase diagram.

Chapter 4 lays out the first set of results, discussing the doping and temperature dependance of the in-plane superfluid density, which displays a linear temperature dependence, confirming d-wave pairing and showing a clear lack of 2- or 3- dimensional critical behaviour. Among the other results discussed are the effects of strong scattering, a sublinear correlation between T_c and ρ_{s0}, and the possibility of a phase transition as the doping is varied. These results challenge existing phenomenology, and will likely form a foundation for the proper understanding of the underdoped cuprate superconductors.

Finally, the results of a two-fluid analysis are discussed, showing a doping independent transport relaxation rate and evidence for a small superconducting gap that is proportional to T_c. This last result has motivated a collaboration with Dr. J. S. Dodge to look for the absorbtion edge using terahertz radiation.

Appendix A

The Cavity Perturbation Approximation

In this appendix it is shown how cavity perturbation can be used to obtain direct measurements of the surface impedance Z_s, the permittivity ϵ, and the permeability μ of small samples placed in the fields of a microwave resonator.[1] The utility of the technique lies in its simplicity — changes in the complex quantities Z_s, ϵ and μ are directly proportional to shifts in the resonant frequency f_0 and bandwidth f_B of the microwave resonator.

The methods of Altshuler[7] and Ormeno *et al.*[45] are used in the following. The subscripts 1 and 2 denote the configurations before and after the perturbation, respectively. Although a continuous wave source is used to sweep out the frequency response of the resonant modes, the experiment is actually probing the free-decay response of the resonator. It is therefore convenient to use a complex-exponential notation in which, for example, the time dependance of the magnetic field is given by $\vec{H}(t) = \Re\{\mathbf{H}e^{i\tilde{\omega}t}\}$. Here $\mathbf{H}$ is a complex phasor vector field and $\tilde{\omega} = \omega' + i\omega''$ is a complex angular frequency with positive imaginary part. The Fourier transform of this time dependance is a Lorentzian centered at $f_0 = \omega'/2\pi$, with full width at half maximum $f_B = \omega''/\pi$.

The integral over the cavity volume

$$\int_V \{\mathbf{E}_1 \cdot \nabla \times \mathbf{H}_2 - \mathbf{H}_2 \cdot \nabla \times \mathbf{E}_1 + \mathbf{H}_1 \cdot \nabla \times \mathbf{E}_2 - \mathbf{E}_2 \cdot \nabla \times \mathbf{H}_1\} \mathrm{d}V \tag{A.1}$$

---

[1] Z_s, ϵ and μ can be treated as scalars, because we usually align the symmetry axes of single crystal samples with the microwave field polarization.

can be converted to a surface integral over the cavity walls using the divergence theorem, resulting in

$$\int_S [\mathbf{H}_2 \times \mathbf{E}_1 - \mathbf{H}_1 \times \mathbf{E}_2] \cdot \hat{\mathbf{n}}\ \mathrm{d}S, \tag{A.2}$$

where $\hat{\mathbf{n}}$ is the outward pointing normal to the surface.

The surface impedance relates the tangential components of the electric and magnetic fields at the surface and is formally defined by

$$\mathbf{E}_t = Z_s \hat{\mathbf{n}} \times \mathbf{H}, \tag{A.3}$$

allowing A.2 to be rewritten as

$$\int_S [Z_{s_1} \mathbf{H}_2 \times (\hat{\mathbf{n}} \times \mathbf{H}_1) - Z_{s_2} \mathbf{H}_1 \times (\hat{\mathbf{n}} \times \mathbf{H}_2)] \cdot \hat{\mathbf{n}}\ \mathrm{d}S. \tag{A.4}$$

Using the identity $\mathbf{A} \times (\mathbf{B} \times \mathbf{C}) = \mathbf{B}(\mathbf{A} \cdot \mathbf{C}) - \mathbf{C}(\mathbf{A} \cdot \mathbf{B})$ this becomes

$$\int_S \Big\{ Z_{s_1} [\hat{\mathbf{n}}(\mathbf{H}_2 \cdot \mathbf{H}_1) - \mathbf{H}_1(\mathbf{H}_2 \cdot \hat{\mathbf{n}})] - Z_{s_2} [\hat{\mathbf{n}}(\mathbf{H}_1 \cdot \mathbf{H}_2) - \mathbf{H}_2(\mathbf{H}_1 \cdot \hat{\mathbf{n}})] \Big\} \cdot \hat{\mathbf{n}}\, \mathrm{d}S. \tag{A.5}$$

The high-frequency fields deep inside the metal surface vanish, which, by continuity of flux, requires $\hat{\mathbf{n}} \cdot \mathbf{H}_{1,2} = 0$. Then

$$\int_S [\mathbf{H}_2 \times \mathbf{E}_1 - \mathbf{H}_1 \times \mathbf{E}_2] \cdot \hat{\mathbf{n}}\, \mathrm{d}S = - \int_S \Delta Z_s \mathbf{H}_1 \cdot \mathbf{H}_2\ \mathrm{d}S, \tag{A.6}$$

showing that A.1 is directly related to a change in the surface impedance of the surface bounding the volume.

The next step is to relate the surface impedance to the complex resonator frequency, and to changes in the electric and magnetic properties of the materials inside the resonator. Faraday's law in phasor form is

$$\nabla \times \mathbf{E}_n = -i\tilde{\omega}_n \mu_n \mathbf{H}_n, \tag{A.7}$$

where $n = 1, 2$. Ampère's law is usually written

$$\nabla \times \mathbf{H}_n = \mathbf{J}_n + i\tilde{\omega}_n \epsilon_n \mathbf{E}_n, \tag{A.8}$$

but here the conduction current density $\mathbf{J}_n = \sigma_n \mathbf{E}_n$ is absorbed into a redefinition of the permittivity,[2] $\epsilon_n \rightarrow \epsilon'_n = \epsilon_n - i\sigma_n/\omega$, so that

$$\nabla \times \mathbf{H}_n = i\tilde{\omega}_n \epsilon'_n \mathbf{E}_n. \tag{A.9}$$

---

[2] This reflects that fact that at finite frequency there is no fundamental difference between free and bound charge. To avoid spurious frequency shifts in the experiment, samples of highly conducting material should be positioned in regions of low electric field.

Substituting Eqs. A.7 and A.9 into A.1 yields

$$\int_V \{\mathbf{E}_2\cdot(i\tilde{\omega}_1\epsilon_1'\mathbf{E}_1)+\mathbf{H}_1\cdot(i\tilde{\omega}_2\mu_2\mathbf{H}_2)-\mathbf{H}_2\cdot(i\tilde{\omega}_1\mu_1\mathbf{H}_1)-\mathbf{E}_1\cdot(i\tilde{\omega}_2\epsilon_2'\mathbf{E}_2)\}\mathrm{d}V \quad \text{(A.10)}$$

$$= -i\int_V \Big\{(\tilde{\omega}_2\epsilon_2'-\tilde{\omega}_1\epsilon_1')\mathbf{E}_1\cdot\mathbf{E}_2+(\tilde{\omega}_1\mu_1-\tilde{\omega}_2\mu_2)\mathbf{H}_1\cdot\mathbf{H}_2\Big\}\mathrm{d}V \quad \text{(A.11)}$$

$$= i\tilde{\omega}_1\int_V[\Delta\epsilon'\mathbf{E}_1\cdot\mathbf{E}_2-\Delta\mu\mathbf{H}_1\cdot\mathbf{H}_2]\mathrm{d}V+i\Delta\tilde{\omega}\int_V[\epsilon_2'\mathbf{E}_1\cdot\mathbf{E}_2-\mu_2\mathbf{H}_1\cdot\mathbf{H}_2]\mathrm{d}V. \quad \text{(A.12)}$$

For small perturbations $\mathbf{E}_1\approx\mathbf{E}_2$ and $\mathbf{H}_1\approx\mathbf{H}_2$. For a high Q resonance $\tilde{\omega}$ is predominantly real so that to good approximation the phase difference between $\mathbf{E}$ and $\mathbf{H}$ is $\pm\frac{\pi}{2}$. Without loss of generality we set the phase of $\mathbf{H}$ to zero, giving the following result:

$$\int_V(\mu_2\mathbf{H}_1\cdot\mathbf{H}_2-\epsilon_2'\mathbf{E}_1\cdot\mathbf{E}_2)\mathrm{d}V\approx\int_V(\mu_2|H|^2+\epsilon_2'|E|^2)\mathrm{d}V=4U, \quad \text{(A.13)}$$

where U is the energy stored in the resonator.

Equating Eq. A.12 to Eq. A.5, substituting Eq. A.13, and solving for $\Delta\tilde{\omega}$ yields the main cavity perturbation result:

$$\Delta f_0+i\Delta f_B/2$$
$$\approx \left\{\frac{i}{2\pi}\int_S\Delta Z_s\mathbf{H_1}\cdot\mathbf{H_2}\mathrm{d}S-f_0\int_V[\Delta\mu\mathbf{H}_1\cdot\mathbf{H}_2+\Delta\epsilon'\mathbf{E}_1\cdot\mathbf{E}_2]\mathrm{d}V\right\}\Big/4U. \quad \text{(A.14)}$$

Bibliography

[1] Cernox$^{\text{TM}}$ resistor, model CX-1050-SD, Lake Shore Cryotronics, 575 McCorke Boulevard, Westerville, Ohio 43082.

[2] Mini-Flex Part No. BC-250-40-14 beryllium–copper bellows, Mini-Flex Corporation, 2472 Eastman Ave. Unit 29, Ventura, California 93003.

[3] Dow Corning No. 976V High Vacuum Grease, Dow Corning Corporation, 3901 S. Saginaw Rd., Midland, Michigan 48640.

[4] eSCeTe Single Crystal Technology, PO Box 3896, Enschede, NL-7500 DW, The Netherlands.

[5] Microlap Technologies, Inc., 213 1st Street NW, Rolla, North Dakota 58367.

[6] ELAN Ltd., 3 Derptsky per. Saint-Petersburg, 198103 Russia.

[7] H. M. Altshuler. Dielectric constant. In *Handbook of Microwave Measurements II*, pages 495–548. Polytechnic Institute of Brooklyn, Brooklyn, N.Y., 1963.

[8] P. W. Anderson. The resonating valence bond state in La_2CuO_4. *Science*, 235:1196, 1987.

[9] J. Bardeen, L. N. Cooper, and J. R. Schrieffer. Theory of superconductivity. *Phys. Rev.*, 108:1175, 1957.

[10] J. G. Bednorz and K. A. Müller. The discovery of a class of high-temperature superconductors. *Zeitschrift fur Physik B*, 64:189, 1986.

[11] D. A. Bonn et al. Comparison of the influence of Ni and Zn impurities on the electromagnetic properties of $YBa_2Cu_3O_{6.95}$. *Phys. Rev. B*, 50:4051, 1994.

[12] D. A. Bonn, D. C. Morgan, and W. N. Hardy. Split-ring resonators for measuring microwave surface-resistance of oxide superconductors. *Rev. Sci. Instrum.*, 62:1819, 1991.

[13] E. W. Carlson, S. A. Kivelson, V. J. Emery, and E. Manousakis. Classical phase fluctuations in high temperature superconductors. *Phys. Rev. Lett.*, 83:612, 1999.

[14] M. J. Case and I. F. Herbut. Screening in anisotropic superfluids and the superfluid density in underdoped cuprates. *Phys. Rev. B*, 72:104503, 2005.

[15] R. J. Corruccini and J. J. Gniewek. *Thermal Expansion of Technical Solids at Low Temperatures: a Compilation from the Literature*. National Bureau of Standards, 1961.

[16] L. Dietl and U. Trinks. The surface-resistance of a superconducting lead tin alloy. *Nucl. Instrum. A*, 284:293, 1989.

[17] D. Duffy, P. J. Hirschfeld, and D. J. Scalapino. Quasiparticle liftimes in a $d_{x^2-y^2}$ superconductor. *Phys. Rev. B*, 64:224522, 2001.

[18] A. C. Durst and P. A. Lee. Impurity-induced quasiparticle transport and universal-limit Wiedemann–Franz violation in *d*-wave superconductors. *Phys. Rev. B*, 62:1270, 2000.

[19] V. J. Emery and S. A. Kivelson. Importance of phase fluctuations in superconductors with small superfluid density. *Nature*, 374:434, 1995.

[20] D. S. Fisher, M. P. A. Fisher, and D. A. Huse. Thermal fluctuations, quenched disorder, phase transitions, and transport in type-II superconductors. *Phys. Rev. B*, 43:130, 1991.

[21] M. Franz and A. P. Iyengar. 4D-XY quantum criticality in a doped Mott insulator. cond-mat/0504735, 2005.

[22] M. Franz and Z. Tešanović. Algebraic fermi liquid from phase fluctuations: "topological" fermions, vortex "berryons," and QED$_3$ theory of cuprate superconductors. *Phys. Rev. Lett.*, 87:257003, 2001.

[23] M. Franz, Z. Tešanović, and O. Vafek. *Phys. Rev. B*, 66:054535, 2002.

[24] W. N. Hardy et al. Precision measurements of the temperature dependence of λ in $YBa_2Cu_3O_{6.95}$: Strong evidence for nodes in the gap function. *Phys. Rev. Lett.*, 70:3999, 1993.

[25] I. F. Herbut. Antiferromagnetism from phase disordering of a *d*-wave superconductor. *Phys. Rev. Lett.*, 88:047006, 2002.

[26] I. F. Herbut. QED$_3$ theory of underdoped high-temperature superconductors. *Phys. Rev. B*, 66:094504, 2002.

[27] I. F. Herbut. Effective theory of high-temperature superconductors. *Phys. Rev. Lett.*, 94:237001, 2005.

[28] I. F. Herbut and M. J. Case. Finite temperature superfluid density in very underdoped cuprates. *Phys. Rev. B*, 70:094516, 2004.

[29] P. J. Hirschfeld and N. Goldenfeld. Effect of strong scattering on the low-temperature penetration depth of a d-wave superconductor. *Phys. Rev. B*, 48:4219, 1993.

[30] P. J. Hirschfeld, W. O. Putikka, and D. J. Scalapino. d-wave model for the microwave response of high-T_c superconductors. *Phys. Rev. B*, 50:10250, 1994.

[31] A. Hosseini, D. M. Broun, D. E. Sheehy, T. P. Davis, M. Franz, W. N. Hardy, Ruixing Liang, and D. A. Bonn. Survival of the d-wave superconducting state near the edge of antiferromagnetism in the cuprate phase diagram. *Phys. Rev. Lett.*, 93:107003, 2004.

[32] A. Hosseini, R. Harris, Saeid Kamal, P. Dosanjh, J. Preston, Ruixing Liang, W. N. Hardy, and D. A. Bonn. Microwave spectroscopy of thermally excited quasiparticles in $YBa_2Cu_3O_{6+x}$. *Phys. Rev. B*, 60:1349, 1999.

[33] L. B. Ioffe and A. I. Larkin. Gapless fermions and gauge fields in dielectrics. *Phys. Rev. B*, 39:8988, 1989.

[34] L. B. Ioffe and A. J. Millis. d-wave superconductivity in doped Mott insulators. *J. Phys. Chem. Solids*, 63:2259, 2002.

[35] A. Kopp and S. Chakravarty. Criticality in correlated quantum matter. *Nat. Phys.*, 1:53, 2005.

[36] P. A. Lee and X. G. Wen. Unusual superconducting state of underdoped cuprates. *Phys. Rev. Lett.*, 78:4111, 1997.

[37] R. Liang, D. A. Bonn, and W. N. Hardy. Growth of high quality YBCO single crystals using $BaZrO_3$ crucibles. *Physica C*, 304:105, 1998.

[38] R. Liang, D. A. Bonn, and W. N. Hardy. Preparation and characterization of homogeneous YBCO single crystals with doping level near the SC–AFM boundary. *Physica C*, 383:1–7, 2002.

[39] R. Liang, D. A. Bonn, and W. N. Hardy. Evaluation of CuO_2 plane hole doping in $YBa_2Cu_3O_{6+x}$ single crystals. cond-mat/0510674, October 2005.

[40] R. Liang, D. A. Bonn, W. N. Hardy, and D. M. Broun. Lower critical field and superfluid density of highly underdoped $YBa_2Cu_3O_{6+x}$ single crystals. *Phys. Rev. Lett.*, 94:117001, 2005.

[41] F. London and H. London. The electromagnetic equations of the supraconductor. *Proc. Roy. Soc.*, A149:71, 1935.

[42] L. F. Mattheiss. Electronic band properties and superconductivity in $La_{2-y}X_yCuO_4$. *Phys. Rev. Lett.*, 58:1028, 1987.

[43] A. J. Millis, S. M. Girvin, L. B. Ioffe, and A. I. Larkin. Anomalous charge dynamics in the superconducting state of underdoped cuprates. *J. Phys. Chem. Solids*, 59:1742, 1998.

[44] J. Orenstein and A. J. Millis. Advances in the physics of high-temperature superconductivity. *Science*, 288:468, 2000.

[45] R. J. Ormeno, D. C. Morgan, D. M. Broun, S. F. Lee, and J. R. Waldram. Sapphire resonator for the measurement of surface impedance of high-temperature superconducting thin films. *Rev. Sci. Instrum.*, 68:2121, 1997.

[46] S. Özcan, P. J. Turner, J. R. Waldram, R. J. Drost, P. H. Kes, and D. M. Broun. Electrical transport measurements in the superconducting state of $Bi_2Sr_2CaCu_2O_{8+x}$ and $Tl_2Ba_2CuO_{6+\delta}$. cond-mat/0508621, 2005.

[47] T. Pereg-Barnea, P. J. Turner, R. Harris, G. K. Mullins, J. S. Bobowski, M. Raudsepp, Ruixing Liang, D. A. Bonn, and W. N. Hardy. Absolute values of the London penetration depth in $YBa_2Cu_3O_{6+x}$ measured by zero-field ESR spectroscopy on Gd-doped single crystals. *Phys. Rev. B*, 69:184513, 2004.

[48] W. H. Press, B. P. Flannery, S. A. Teukolsky, and W. T. Vetterling. *Numerical Recipes in C: The Art of Scientific Computing.* Cambridge University Press, 2^{nd} edition, 1992.

[49] D. E. Sheehy, T. P. Davis, and M. Franz. Unified theory of the ab-plane and c-axis penetration depths of underdoped cuprates. *Phys. Rev. B*, 70:054510, 2004.

[50] J. E. Sonier, F. D. Callaghan, J. H. Brewer, W. N. Hardy, D. A. Bonn, and R. Liang. Doping dependence of the μsr lineshape in $YBa_2Cu_3O_y$ crystals: Strong evidence for y=6.0 antiferromagnetism in the vortex cores of y=6.50. cond-mat/0508079, 2005.

[51] S. Sridhar and W. L. Kennedy. Novel technique to measure the microwave response of high $T_c$superconductors between 4.2 and 200 K. *Rev. Sci. Instrum.*, 59:531, 1988.

[52] C. Stock, W. J. L. Buyers, Z. Yamani, C. L. Broholm, J.H. Chung, Z. Tun, R. Liang, D. Bonn, W. N. Hardy, and R. J. Birgeneau. Central mode and spin confinement near the boundary of the superconducting phase in $YBa_2Cu_3O_{6.353}$ (T_c=18 k). cond-mat/0505083, 2005.

[53] C. C. Tsuei and J. R. Kirtley. Pairing symmetry in cuprate superconductors. *Rev. Mod. Phys.*, 72:969, 2000.

[54] B. W. Veal, A. P. Paulikas, Hoydoo You, Hao Shi, Y. Fang, and J. W. Downey. Observation of temperature-dependent site disorder in $YBa_2Cu_3O_{7-\delta}$ below 150 °C. *Phys. Rev. B*, 42:6305, 1990.

[55] J. R. Waldram, P. Theopistou, A. Porch, and H. M. Cheah. Two-fluid interpretation of the microwave conductivity of $YBa_2Cu_3O_{7-\delta}$. *Phys. Rev. B*, 55:3222, 1997.

[56] X. G. Wen and P. A. Lee. Theory of quasiparticles in the underdoped high-T_c superconducting state. *Phys. Rev. Lett.*, 80:2193, 1998.

[57] Z. A. Xu, N. P. Ong, Y. Wang, T. Kakeshita, and S. Uchida. Vortex-like excitations and the onset of superconducting phase fluctuation in underdoped $\mathrm{La}_{2-x}\mathrm{Sr}_x\mathrm{CuO}_4$. *Nature*, 406:486, 2000.

[58] Jaejun Yu, A. J. Freeman, and J. H. Xu. Electronically driven instabilities and superconductivity in the layered $\mathrm{La}_{2-x}\mathrm{Ba}_x\mathrm{CuO}_4$ perovskites. *Phys. Rev. Lett.*, 58:1035, 1987.

[59] J. Zaanen, A. T. Paxton, O. Jepsen, and O. K. Anderson. Chain-fragment doping and the phase diagram of $\mathrm{YBa}_2\mathrm{Cu}_3\mathrm{O}_{6+x}$. *Phys. Rev. Lett.*, 60:2685, 1988.

[60] X. J. Zhou et al. Universal nodal Fermi velocity. *Nature*, 423:398, 2003.

[61] Y. Zuev, M. S. Kim, and T. R. Lemberger. Correlation between superfluid density and T_c of underdoped $\mathrm{YBa}_2\mathrm{Cu}_3\mathrm{O}_{6+x}$ near the superconductor-insulator transition. *Phys. Rev. Lett.*, 95:137002, 2005.

[62] Y. Zuev, J. A. Skinta, M. S. Kim, T. R. Lemberger, E. Wertz, K. Wu, and Q. Li. The role of thermal phase fluctuations in underdoped $\mathrm{YBa}_2\mathrm{Cu}_3\mathrm{O}_{6+x}$ films. cond-mat/0407113, 2004.